Investigating the Southern Ocean Biogeochemical Divide

Thanyaphon Bumrungsri

Tomas Torsvik and Are Olsen

Master's Thesis in Marine Biogeochemistry
Geophysical Institute
University of Bergen

May 31, 2024

Acknowledgements

I would like to express my gratitude to Prof. Christoph Heinze for initiating the idea about the Southern Ocean Biogeochemical Divide. I am deeply thankful to my advisor, Are Olsen, for his support, invaluable guidance, and valuable feedback. Special thanks to my main advisor, Tomas Torsvik, for his dedication and patience. His advice and assistance throughout the process, particularly in mastering coding, have been immensely helpful.

I also wish to acknowledge all the researchers who have worked in the fields of biogeochemistry in the Southern Ocean and climate science. Your contributions have been fundamental to my study.

Lastly, I thank my family, my boyfriend, and my friends for their mental support and encouragement. Your belief in me has been a source of strength and motivation.

In my masters thesis, I utilized AI tools to enhance my work. For grammar checks, I employed Grammarly (https://app.grammarly.com). For paraphrasing, I used QuillBot (https://quillbot.com). Additionally, I relied on ChatGPT (https://chatgpt.com) to assist with debugging my code.

Thanyaphon Bumrungsri
Bergen, 31 May 2024

Abstract

The Southern Ocean plays a crucial role in Earth's climate and biogeochemical (BGC) cycles due to its unique features, such as strong westerly winds, intense ocean circulation, and its high-latitude location. This study focuses on the Southern Ocean Biogeochemical Divide (SOBD), a region where distinct ocean circulation patterns significantly influence nutrient distribution, marine primary production, and carbon sequestration. Utilizing data from the Norwegian Earth System Model version 2 (NorESM2-MM) and observational data from the World Ocean Atlas 2018 (WOA18), we examine the spatial and temporal variability of key BGC tracers—phosphate (PO_4), dissolved oxygen (DO), and silicate (Si). Our analysis reveals that PO_4 concentrations show a clear latitudinal gradient with higher levels near the Antarctic continent. DO concentrations are higher near the Antarctic continent at the surface, decreasing with depth. Si concentrations display similar patterns to PO_4 but with generally higher values. The SOBD is identified as a consistent feature of upwelling water at approximately 250m depth, where significant changes in nutrient concentrations align with the 1036.5 kg/m^3 isopycnal line, marking the transition between different water masses. This alignment helps identify the SOBD's location, which falls between the Polar Front (PF) and the Southern Boundary (SB) of the Antarctic Circumpolar Current (ACC). Time series analysis highlights significant temporal fluctuations in BGC tracer concentrations, with notable shifts around the mid-20th century. These shifts are associated with the Early Twentieth Century Warming (ETCW) and changes in the Southern Annular Mode (SAM) index, influencing the strength of westerly winds and upwelling processes. Despite these fluctuations, the SOBD location remains stable over the study period (1850 to 2014).

List of Abbreviations

AABW Antarctic Bottom Water

AAIW Antarctic Intermediate Water

ACC Antarctic Circumpolar Current

BGC Biogeochemical

$CaCO_3$ Calcium Carbonate

CESM Community Earth System Model

CDW Circumpolar Deep Water

CMIP6 Coupled Model Intercomparison Project

CMOR Climate Model Output Rewriter

CO_2 Carbon Dioxide

DMS Dimethyl Sulfide

DO Dissolved Oxygen

DSi Dissolved Silica

ETCW Early Twentieth Century Warming

iHAMOCC Isopycnic Coordinate Hamburg Ocean Carbon Cycle

MOC Meridional Overturning Circulation

NADW North Atlantic Deep Water

NorESM2 Norwegian Earth System Model Version 2

NPZD Nutrient Phytoplankton Zooplankton Detritus

O_2 Oxygen

OCMIP Ocean Carbon Cycle Model Intercomparison Project

P Phosphorus

pCO_2 Partial Pressure of Carbon Dioxide

PF Polar Front

piControl Pre-industrial Control

PO_4 Phosphate

SAF Subantarctic Front

SACCF Southern Antarctic Circumpolar Current Front

SAM Southern Annular Mode

SAMW Subantarctic Mode Water

SB Southern Boundary

Si Silicate

SOBD Southern Ocean Biogeochemical Divide

WOA18 World Ocean Atlas 2018

Contents

List of Figures

Chapter 1

Introduction

The Southern Ocean is the vast expanse of water surrounding Antarctica. This ocean stands out as a unique and highly dynamic region in the world's ocean system. The unique features and impacts of the Southern Ocean on Earth's climate and biogeochemical (BGC) cycles are shaped by several factors, such as its strong westerly winds, intense ocean circulation, and location at high latitudes (*Iudicone et al.*, 2008; *Marinov et al.*, 2006; *Primeau et al.*, 2013; *Sarmiento et al.*, 2004).

The powerful westerly winds drive the Antarctic Circumpolar Current (ACC), the world's largest ocean current, which circulates around Antarctica and connects the Atlantic, Pacific, and Indian Oceans (*Williams*, 2015). This intense circulation, along with the upwelling of deep, nutrient-rich waters, creates an environment that fosters high primary productivity. Primary productivity is the process by which photosynthetic organisms like phytoplankton convert inorganic carbon, mainly carbon dioxide (CO_2), into organic matter. This process not only supports a rich and diverse marine ecosystem but also helps regulate atmospheric CO_2 levels by sequestering carbon in the ocean's interior (*Kaiser et al.*, 2011).

One of the key features of the Southern Ocean is the Southern Ocean Biogeochemical Divide (SOBD), a region marked by a distinct separation in ocean circulation patterns that significantly influences nutrient distribution, marine primary production, and carbon sequestration (*Marinov et al.*, 2006; *Xie et al.*, 2022). This divide is thought to be maintained by the strong winds and currents that encircle Antarctica, which isolate the surface waters from the deeper waters (*Mazloff et al.*, 2010). The distribution of nutrients in this region is closely linked to the pattern of the meridional overturning circulation (MOC). Upwelling of Circumpolar Deep Water (CDW) transports nutrient-rich water masses to the surface within the ACC (*Marshall and Speer*, 2012; *Tamsitt et al.*, 2017) (shown in Figure 1.1). This process creates two circulation cells at the surface of the Southern Ocean. The lower cell involves water that flows southward, carrying upwelled CDW that loses buoyancy and sinks to great depths, forming Antarctic Bottom Water (AABW). This dense water mass is vital for global ocean circulation as it moves northward into the Atlantic, Pacific, and Indian basins. In contrast, the upper cell involves northward-flowing CDW that forms Antarctic Intermediate Water (AAIW) and Subantarctic Mode Water (SAMW). These water masses are crucial for the Southern Ocean's BGC cycles because they carry nutrients and dissolved gases into lower latitudes of the global oceans through subsurface layers (*Sallée et al.*, 2010; *Talley et al.*, 2011). The boundary between the upper and lower cells is referred to as the SOBD

(*Marinov et al.*, 2006).

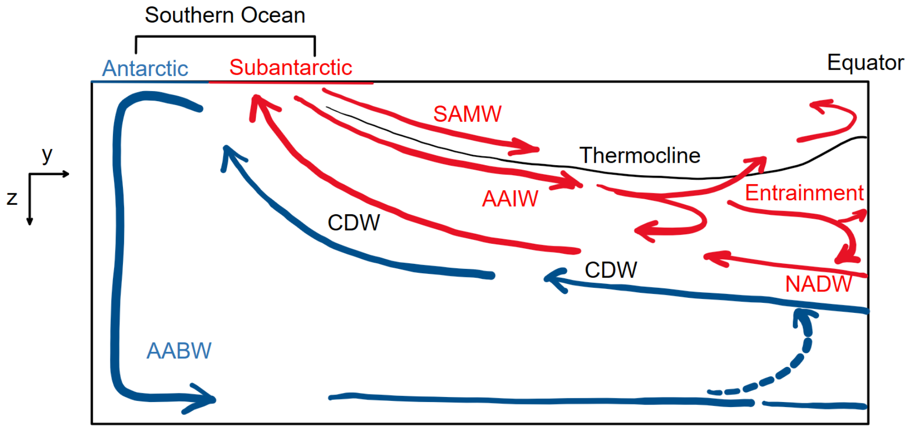

Figure 1.1: Illustration of the meridional overturning circulation (MOC) in the Southern Ocean. Upwelled Circumpolar Deep Water (CDW) is either advected northward, contributing to the upper circulation (red), or moves southward into the lower circulation (blue). The Antarctic Polar Front marks the boundary between the Antarctic and Subantarctic regions. AABW, Antarctic Bottom Water; AAIW, Antarctic Intermediate Water; NADW, North Atlantic Deep Water; SAMW, Subantarctic Mode Water. Modified figure from Marinov et al. (2006).

To understand the SOBD, it is important to consider the role of biological pump efficiency, the process behind this divide (*Marinov et al.*, 2006). The biological carbon pump is primarily driven by the photosynthetic production of organic matter at the ocean's surface and its subsequent transport to deeper layers, where it undergoes remineralization. 'Remineralized nutrients' refer to nutrients added to the ocean interior through this process, while 'preformed nutrients' are those that remain biologically unused at the surface and are transported to the ocean interior via newly formed deep water. The biological pump decreases the concentration of preformed nutrients at the surface by converting them into export production, thereby increasing the concentration of remineralized nutrients in the deeper ocean. Due to the link between nutrients and carbon in both photosynthesis and remineralization, a more efficient conversion of preformed to remineralized nutrients enhances the biological pump's ability to sequester carbon in the deep ocean, thereby reducing atmospheric pCO_2 (*Ito and Follows*, 2005). At the SOBD, the dynamics of this conversion process could reveal variations in nutrient usage and carbon transport mechanisms across different latitudinal zones, offering insights into how the Southern Ocean modulates global BGC cycles and influences climate change mitigation.

We use marine BGC data to identify the SOBD and the variation over time. Our study focus on the changes in phosphate (PO_4), dissolved oxygen (DO), and silicate (Si) levels. PO_4 is an essential nutrient for phytoplankton, and it plays a crucial role in the primary productivity of the ocean (*Lin et al.*, 2016). The concentration of oxygen (O_2) in the ocean provides constraints on the efficiency of the biological pump that mediates the sequestration of carbon in the deep ocean (*Buesseler and Boyd*, 2009; *Devol and Hartnett*, 2001; *Honjo et al.*, 2008) and influences the biological communities (*Sarmiento*, 2006; *Stramma et al.*, 2012). Similarly, Si is a vital nutrient, especially for diatoms, a group of phytoplankton that forms the basis of marine food webs (*Smetacek*, 1998).

The relevance of the SOBD to the marine nutrient and carbon cycle has been evaluated through BGC modeling (*Holzer et al.*, 2014; *Marinov et al.*, 2006; *Primeau et al.*, 2013). A recent study by *Xie et al.* (2022) identified an approximate location of the SOBD. However, none of these studies have examined its variability over long time spans. The main objective of our study is to use the Norwegian Earth System Model version 2 (NorESM2) to explore the SOBD location and its variability from 1850–2014. NorESM2 offers a comprehensive representation of ocean and atmospheric systems, providing high-resolution outputs that facilitate an in-depth examination of the SOBD over time and space. This study aims to determine if the SOBD can be reliably identified in a global climate model with approximately 1-degree horizontal resolution, unlike previous studies that primarily utilized higher-resolution regional models where sharp fronts are more easily represented. Additionally, we aim to investigate the stability of the SOBD over an extended period, leveraging the long time span feature of climate models that process-oriented studies do not capture. Furthermore, the study will explore the evolution of BGC tracers in the SOBD regions of the Atlantic, Pacific, and Indian oceans. By focusing on NorESM2, this research assesses the model's capabilities and limitations in capturing the dynamics and characteristics of the SOBD.

As this introduction has set the stage for our exploration of the SOBD, the following chapters of this thesis will delve deeper into the subject to fulfill the research objectives. Chapter 2 provides the theoretical background, grounding the study in existing literature. Chapter 3 outlines the methodologies used in the analysis, detailing the data sources, analytical techniques, and approaches for synthesizing and interpreting the data. Chapter 4 presents the results from the analysis and discusses these findings in the context of BGC and physical dynamics. Finally, Chapter 5 serves as the conclusion, synthesizing the findings to discuss their implications for future research and the potential applications of the study's outcomes.

Chapter 2

Background

2.1 The Southern Ocean

The Southern Ocean is the broad ocean region surrounding Antarctica. The bathymetry that underlies the Southern Ocean is a mixture of comparatively smooth, oceanic abyssal plains of up to ∼4000m depth or deeper, separated by much shallower and often convoluted ridge systems (Figure 2.1). The overall topographic configuration of the Southern Ocean is unique in the world, possessing a circumpolar channel that is open at all longitudes. This, combined with the strong westerly winds and buoyancy forcing that typifies the high latitudes, leads to the existence of the ACC (Figure 2.1b) (*Rintoul et al.*, 2001).

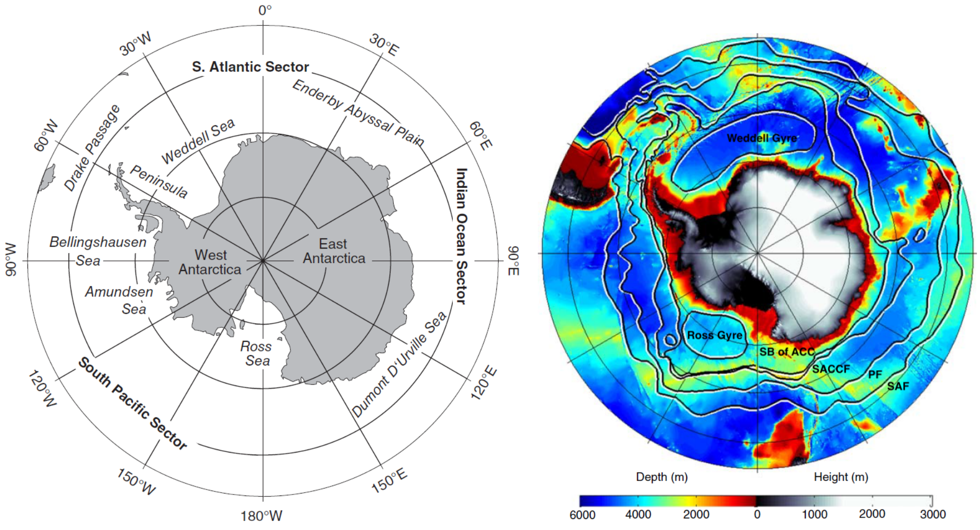

(a) *(b)*

Figure 2.1: Map (a) and Bathymetry/Topography (b) of the Southern Ocean and Antarctica. Depths below sea level are coloured; heights above sea level are monochrome. Note the convoluted ridge systems, such as in and around Drake Passage, separating wide expanses of oceanic abyssal plain. Also shown are schematic depictions of the fronts of the Southern Ocean: the Subantarctic Front (SAF), the Polar Front (PF), the Southern ACC Front (SACCF), and the Southern Boundary (SB) of the ACC (Orsi et al., 1995). Poleward of the ACC lie sub-polar gyre systems, including the Weddell and Ross Gyres. Figure source: Meredith and Brandon (2017).

The ACC is the largest current system in the world, continuously transporting approximately 130 Sv of water eastwards around Antarctica (1 Sv = $10^6 m^3/s$) (*Meredith et al.*, 2011). It is a banded structure, consisting of relatively fast-moving jets separated by more quiescent zones of water. These jets coincide with oceanic fronts, namely (north to south), the Subantarctic Front, the Polar Front and the Southern ACC Front (*Orsi et al.*, 1995). The southern edge of the ACC is marked by the Southern Boundary (SB) (Figure 2.1). Poleward of the ACC lie a series of sub-polar gyres, most notably in the Weddell Sea and Ross Sea (Figure 2.1). These transport a few tens of Sv cyclonically around the basins within which they reside, with the strongest parts of the circulation focused in boundary currents that lie adjacent to the periphery of the basins (*Fahrbach et al.*, 1994).

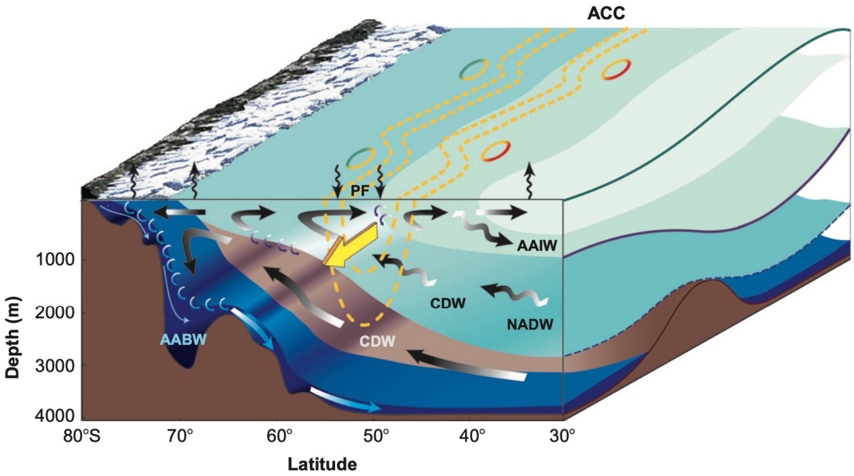

Figure 2.2: A schematic view of the Southern Ocean circulation. The heavy yellow arrow and dashed yellow lines denote the eastward flow of the ACC. The overturning circulation is indicated by dark arrows, with wavy arrows intended to represent transport by eddies. The meridional transport is largely along layers of constant density, represented by the colored surfaces. Vertical curly arrows at the sea surface indicate air-sea buoyancy exchange (upward arrows mean a buoyancy loss by the ocean). Small light arrows show diapycnal mixing. The east-west section on the right face of the diagram illustrates the surface and isopycnal tilts in relation to bottom topography (brown) associated with interfacial and bottom form stress. From Olbers and Visbeck (2005), adapted from Speer et al. (2000).

The strong eastward flow of the ACC has several important implications for the global ocean circulation and its influence on regional and global climate. It promotes exchange between the three major ocean basins, allowing transmission of climate signals and smoothing out zonal differences in water properties, yet inhibits north-south exchange and isolates Antarctica from the warm waters to the north by a strong, continuous eastward flow that acts as a physical barrier. It is reinforced by sharp temperature and salinity fronts, strong westerly winds, and significant eddy activity. The interbasin connection allows the establishment of a global-scale overturning circulation, which transports heat, moisture, and inorganic carbon around the globe and strongly influences the Earths climate. The eastward geostrophic flow of the ACC is associated with steeply sloping density surfaces, which shoal to the south across the current and expose dense waters to the surface in the high-latitude Southern Ocean (Figure 2.2). Where the dense waters outcrop at the sea surface, they exchange heat, moisture, and gases like O_2 and CO_2 with the atmosphere. In this sense, the Southern Ocean acts as a valve regulating exchange between the deep and shallow layers of the global ocean. Upwelling of deep water returns nutrients and carbon to the upper ocean, while sinking of waters from the surface transfers O_2 and anthropogenic CO_2 into the ocean interior. As a result of the vigorous overturning circulation, the Southern Ocean stores large amounts of heat and anthropogenic CO_2. For example, 40% of the total ocean inventory of anthropogenic CO_2 entered the ocean south of 40°S (*Davila et al.*, 2022; *Khatiwala et al.*, 2009, 2013).

The Southern Ocean overturning circulation consists of two cells (Figure 2.2). CDW spreads poleward and shoals, ultimately outcropping at the sea surface. The relatively dense Lower CDW upwells to the south of the ACC, where interactions with the atmosphere and sea ice convert the upwelled water to dense AABW, forming the lower cell of the overturning circulation. AABW sinks and flows along the ocean bottom, spreading northward into the other ocean basins. This deep water mass sequesters carbon and nutrients for centuries to millennia before it gradually upwells in various regions of the world's oceans, influencing global climate and nutrient distribution. Relatively light Upper CDW outcrops within the ACC belt, where it is driven equatorward in the Ekman layer and converted to less dense intermediate waters (AAIW and SAMW) by heat and freshwater gain from the atmosphere, forming the upper cell. AAIW and SAMW are subducted into the ocean's thermocline and spread equatorward at mid-depths. These intermediate waters play a vital role in supplying nutrients to the low-latitude surface ocean, supporting marine productivity far from their origin. In this way, the Southern Ocean connects the upper and lower layers of the ocean and allows a global-scale overturning circulation to exist even in the limit of very weak diapycnal mixing in the ocean interior (e.g., *Speer et al.* (2000)).

2.2 The Role of the Southern Ocean in Climate and Biogeochemical Cycles

The study of biogeochemistry—encompassing the cycling of chemical elements through living systems within their physical, chemical, biological, and geological environments—is integral to Earth's functionality. Within this sphere, the Southern Ocean emerges as a significant influencer, shaping regional ecosystem operations and gas exchange between sea and air. It modulates our planets climate from seasonal-to-millennial timescales, absorbing atmospheric CO_2 through the solubility and biological pump processes while also reintroducing CO_2 from the deep ocean (e.g., *Gruber et al.* (2009); *Sarmiento and Le Quere* (1996); *Sigman et al.* (2010); *Takahashi et al.* (2009)). Furthermore, mode and intermediate water masses that form in the Subantarctic region crucially dictate primary production and carbon export across the world's oceans. They set the biogeochemistry of the global thermocline—a subsurface layer marked by a sharp temperature gradient—which in turn furnishes the upper ocean layers with essential nutrients (*Marinov et al.*, 2006; *Moore et al.*, 2018; *Sarmiento et al.*, 2004). This nuanced interplay underscores the Southern Ocean's pivotal role in global BGC cycling, marking it as a critical component in the Earth's climatic equilibrium.

2.2.1 Carbon Sequestration and Atmospheric Carbon Dioxide Regulation

The Solubility Pump, Biological Pump, and Upwelling

The Southern Ocean is a globally important region for ocean ventilation and the sea-air exchange of CO_2 and other climate-active gases, influenced by complex interactions between physical, chemical, and biological processes (*Marinov et al.*, 2006). The solubility pump, whereby atmospheric CO_2 is taken up by dissolution into surface waters and subsequently subducted into the subsurface, exporting CO_2 into the ocean interior, is particularly strong in the high southern latitudes due to cold surface waters and deep and intermediate water mass formation (e.g., *Gruber et al.* (2019); *Sabine et al.* (2004); *van Heuven et al.* (2014)). However, in the upwelling zones, strong upwelling brings CO_2-rich deep waters to the surface, increasing pCO_2 in surface waters, altering the carbonate system equilibrium and driving CO_2 release to the atmosphere (e.g., *Chapman et al.* (2020); *Pardo et al.* (2017)). A schematic depicting the meridional circulation and the carbon cycle in the Southern Ocean shows in Figure 2.3. The biological pump is also important in the Southern Ocean, particularly during spring and summer (e.g., *Cavan et al.* (2019); *DeVries et al.* (2012); *Ducklow et al.* (2001)). CO_2 is converted into organic carbon during photosynthesis by phytoplankton and other primary producers, stored in plant and animal tissues and subsequently exported to the deep ocean and seafloor when microalgae and other organisms die (*Henley et al.*, 2020). The balance between solubility and biological pump processes and upwelling processes, and their combined effect on the difference between seawater and atmospheric pCO_2 (ΔpCO_2), determine whether the surface ocean behaves as a CO_2 sink or source. The magnitude of CO_2 fluxes depends on combination of the air-sea pCO_2 difference and wind speed, which strongly affects the sea-air gas transfer velocity (e.g., *Fay et al.* (2014); *Wanninkhof* (2014)).

Net Carbon Dioxide Sink Behavior of the Southern Ocean

The Southern Ocean between 30°S and 50°S is currently a major net annual sink for atmospheric CO_2 since biological uptake during summer and solubility pump processes exceed CO_2 outgassing driven by upwelling and vertical mixing predominantly during winter (e.g., *Roobaert et al.* (2019); *Takahashi et al.* (2012)). The Southern Ocean CO_2 sink has taken up approximately 40% of the total oceanic uptake of anthropogenic CO_2 (*DeVries*, 2014; *Fletcher et al.*, 2006; *Orr et al.*, 2001), increasing surface water pCO_2 and causing ocean acidification (*Henley et al.*, 2020). Export of CO_2 to the deep Southern Ocean occurs in specific locations and depends on the interactions between physical properties, such as mixed layer depth, ocean currents, fronts, eddies and winds, all of which are potentially sensitive to climate variability and change, and with bathymetric features (*Chapman et al.*, 2020; *Sallée et al.*, 2012).

Key Controls on Biological Carbon Uptake and Export

Primary production have a significant impact on the contribution of biological carbon uptake, export, and storage in organisms to the Southern Ocean carbon sink. Although primary production is limited by iron availability over much of the Southern

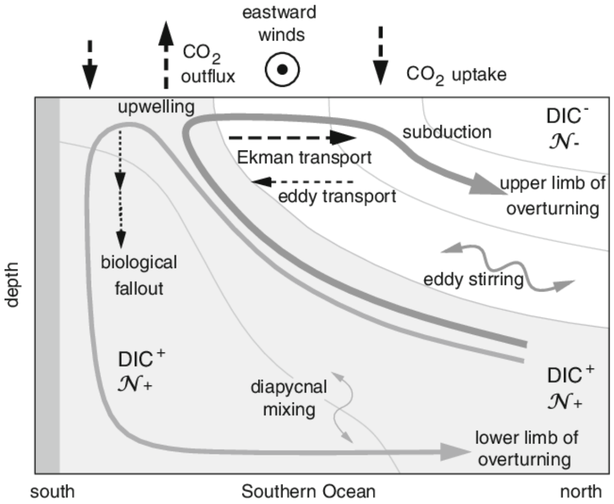

Figure 2.3: The relatively dense Lower CDW upwells to the south of the ACC, where interactions with the atmosphere and sea ice convert the upwelled water to dense AABW, forming the lower cell of the overturning circulation (thin grey line). Relatively light Upper CDW outcrops within the ACC belt, where it is driven equatorward in the Ekman layer and converted to less dense intermediate waters (AAIW and SAMW) by heat and freshwater gain from the atmosphere, forming the upper cell (thick grey line). The nutrient (N) and dissolved inorganic carbon (DIC) have high concentrations at depth from regeneration of biological fallout. Upwelling of carbon-rich waters leads to an outflux of carbon to the atmosphere. Conversely, there is a carbon uptake where mode waters are subducted along the northern flank of the ACC and also where dense bottom waters form at higher latitudes. From Lauderdale et al. (2013), redrawn from Williams and Follows (2011).

Ocean, hotspots of productivity around and downstream of Subantarctic islands and submerged plateaus (e.g., South Georgia, Kerguelen, Crozet), in upwelling and mixing zones, coastal/shelf areas, and the sea ice zone where iron is not limiting, can lead to substantial export of organic carbon to deep waters and/or sediments (*Henley et al.*, 2020).

2.2.2 Global Nutrient Cycles and Phytoplankton Nutrition

The Southern Ocean significantly contributes to global nutrient cycles, enhancing phytoplankton nutrition and productivity. Remarkably, phytoplankton in this region account for approximately 25% of the world's marine primary production, equivalent to 11.4 Pg C yr^{-1} (*Okin et al.*, 2011). This productivity is primarily sustained by the ocean's unique nutrient dynamics.

Iron (Fe), crucial for phytoplankton growth, is the primary limiting nutrient across the Southern Ocean (*de Baar et al.*, 1995; *Watson et al.*, 2000), constrained by minimal atmospheric deposition and the remoteness from terrigenous sources (*Boyd and Ellwood*, 2010). Consequently, during the growing season, phytoplankton production does not fully utilize the available nutrients in the euphotic zone, resulting in lower-than-expected phytoplankton biomass and relatively high concentrations of unused nutrients. This makes the Southern Ocean well known as a high-nutrient, low-chlorophyll (HNLC) region (*Boyd*, 2002; *de Baar et al.*, 1995).

Macronutrients such as nitrate (NO_3), PO_4, and silicic acid play essential roles in supporting the growth and survival of diatoms, with nitrate and phosphate also necessary for other phytoplankton classes for cellular metabolism. The ratio of utilisation between nitrogen (N) and phosphorus (P) deviates from the *Redfield* (1958) ratio of 16:1 across the Southern Ocean according to changes in community composition (*Henley et al.*, 2020; *Weber and Deutsch*, 2010). Unlike much of the global ocean, high rates of macronutrient supply from the CDW prevent widespread N or P limitation in the Southern Ocean except in periods of intense summer growth in high-productivity coastal regions (*Henley et al.*, 2017). These nutrients are critical not only for local BGC processes but also affect global nutrient and carbon cycles (*Moore et al.*, 2018; *Sarmiento et al.*, 2004). In particular, surface nutrient concentrations and ratios in the formation regions of the SAMW and AAIW formation are transported northward by these water masses and mixed through the thermocline into macronutrient-limited surface waters north of 30°S (*Marinov et al.*, 2006). Also a major exporter of nutrients to the AABW, mainly formed in the Weddell and Ross Sea, exports nutrients to deeper waters of the Atlantic, Indian and Pacific oceans. *Sarmiento et al.* (2004) showed that three quarters of the primary production in surface waters north of 30°S is supported by inputs from the Southern Ocean, so that the Southern Ocean can be envisioned as a strong nutrients exporter.

Primary production in the Southern Ocean is dominated by diatoms—phytoplankton with opaline cell walls that thrive in dynamic, highly seasonal, and competitive environments (*Margalef*, 1978). These waters, enriched in Si due to deep-water upwelling, support diatoms that are heavily silicified (*Baines et al.*, 2010). As a result, they deplete Si much more rapidly than other major nutrients such as NO_3 and PO_4. Consequently, as surface waters move northward across the fronts of the ACC, silicon is depleted more rapidly (i.e., further south) than NO_3 or PO_4 (see Figure 2.4).

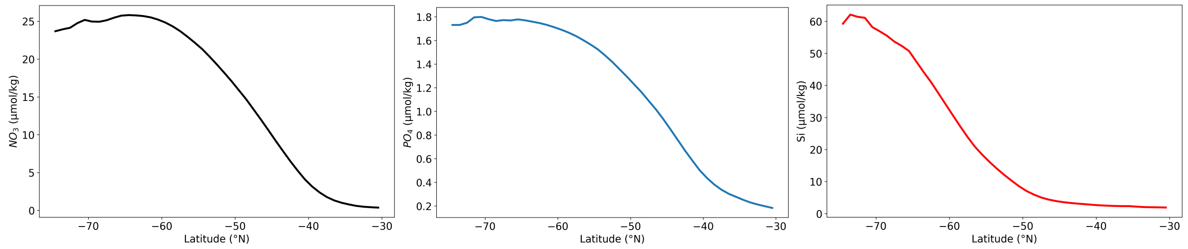

(a) *(b)* *(c)*

Figure 2.4: Latitudinal variation in (a) NO_3, (b) PO_4, and (c) Si in the surface Southern Ocean. Data from WOA18 (1900–2017).

2.2.3 Biogeochemical Tracers in Understanding the Southern Ocean Dynamics

Phosphate

The distribution of PO_4 in the ocean is controlled by a wide range of processes. In the absence of major external sources (Figure 2.5), internal processes are the main drivers, namely the physical circulation and the marine biology. PO_4 is incorporated into organic matter by photosynthetic phytoplankton in the euphotic zone. A fraction of this organic matter escapes recycling in the surface layer and is exported into the ocean interior. Remineralisation of organic matter by bacteria and zooplankton releases nutrients such as PO_4 and consumes O_2. This PO_4 is called regenerated PO_4. The remaining PO_4 is the biotically unutilized surface PO_4, which enters the ocean by subduction during water mass formation, and is called preformed PO_4. According to observational estimates, the preformed phosphate makes up for about 60% of the global oceans PO_4 inventory, whereas regenerated PO_4 derived from remineralisation of organic matter makes up for the remaining 40% (*Ito and Follows*, 2005).

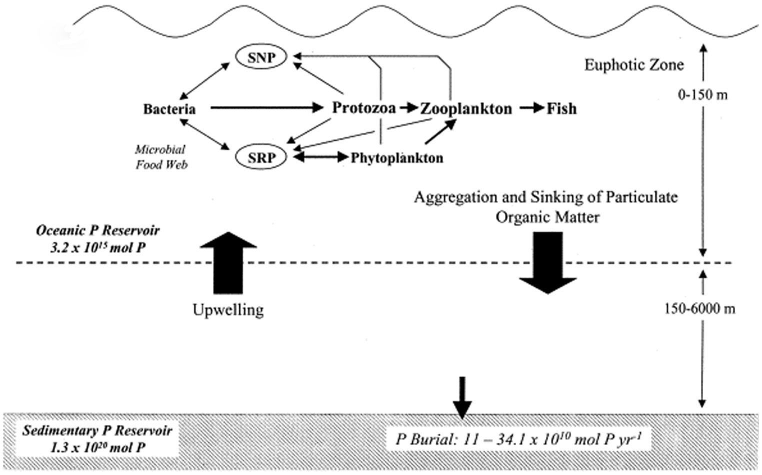

Figure 2.5: The marine P cycle in absence of major external sources. Adapted from Benitez-Nelson (2000).

Patterns of PO_4 concentrations as well as the partitioning into preformed and regenerated components are sensitive to ocean circulation, export production and remineralisation length scale (*Duteil et al.*, 2012). For example, a more active biology increases the transfer of PO_4 from surface to intermediate depths by remineralisation, depleting surface nutrients. Consequently, the amount of PO_4 subducted at high latitudes, i.e. the preformed PO_4, decreases as well. As another example, a more vigorous overturning (at the Southern Ocean) results in higher supply rates of nutrients from the deep ocean to the euphotic zone, which will increase surface nutrient levels. Thereby, the preformed PO_4 pool increases whereas the regenerated PO_4 pool decreases. The global PO_4 distribution is characterized by generally low PO_4 values in surface waters and high concentrations in the deep ocean, with maximum concentrations often found in intermediate waters associated with low oxygen concentrations. However, the Southern Ocean is an exception, where surface waters exhibit relatively high PO_4 concentrations due to upwelling and limited biological utilization.

Dissolved Oxygen

DO is a key indicator for monitoring the marine ecosystem functioning because it is the result of several atmospheric, hydrodynamic, and BGC driving processes (such as air-sea fluxes, vertical convection and mixing, horizontal transport, and biological production and consumption (*Keeling and Garcia*, 2002; *Oschlies et al.*, 2018; *Pitcher et al.*, 2021)). Biochemical processes include sources and sinks of O_2 due to marine production, respiration, and oxidation of organic matter. Physical processes include mass transfer of O_2 caused by water mass ventilation, air-sea gas exchange, gas solubility changes, and mixing by advection and diffusion. The oceanic O_2 inventory is sensitive to changes driven by the physical and biological state of the ocean as well as anthropogenic impacts acting on different time and spatial scales (e.g., *Hofmann and Schellnhuber* (2009); *Keeling and Garcia* (2002); *Matear and Hirst* (2003)). Global O_2 changes in the ocean can be substantial. For example, *Schmidtko et al.* (2017) suggested that the global ocean O_2 inventory has decreased by about 2% since 1960 due to a warming induced decrease in solubility and biological consumption. Oceanic DO is supplied from air-sea exchange and photosynthesis in the euphotic zone, and it is consumed by organic carbon respiration throughout the water column. Because respired carbon accumulation and O_2 consumption are stoichiometrically (fixed ratios of carbon accumulation and O_2 consumption) linked during organic carbon degradation, DO reconstructions are particularly valuable for understanding marine respired carbon storage (*Jaccard et al.*, 2016), which plays a major role in the variability of the pCO_2.

O_2 content is highest at the surface for two main reasons; this is where O_2 dissolves into the ocean from the atmosphere, and the surface water is where O_2 is produced by phytoplankton through photosynthesis. Respiration is also occurring in the surface waters, but the rate of photosynthetic O_2 production is greater than the rate of removal through respiration. It should be noted that even though DO is highest at the surface, there is still far less O_2 in the water than is found in the air. Well-oxygenated surface water may only contain around 8 mg O_2/l, while the air contains 210 mg O_2/l (*Webb*, 2023).

As depth increases, DO declines, reaching a minimum between a few hundred meters and 1000m deep, the aptly-named O_2 minimum layer. At these depths and below, the water is too far removed from the surface for any atmospheric exchange, and there is not enough light to support photosynthesis, so there is little if any O_2 added to the water. At the same time, O_2 is removed from the water through the respiration of deep water organisms, and the decomposition of organic material by bacteria as it sinks to depth.

Below the O_2 minimum layer there is often an increase in DO at the greatest depths. This bottom water is usually colder than the surface water and is under enormous pressure; as stated above, lower temperatures and higher pressure increase the solubility of dissolved gases. But there is another reason that bottom water contains more O_2 than mid-water depths that has to do with the way water circulates throughout the deep ocean. In polar regions, the cold surface water absorbs lots of O_2. This cold, O_2-rich water sinks to the bottom due to its high density, taking the O_2 with it (i.e., AABW in the Southern Ocean). The O_2-rich bottom water will then spend the next thousand years or so moving over the seafloor throughout the major ocean basins. This deep water circulation is the source of O_2 for bottom-dwelling (benthic) organisms. The O_2-rich bottom water forms in the polar regions of the Atlantic, and slowly makes its way to the Pacific, with O_2 being removed for respiration along the way. This is why DO levels in Pacific deep water are generally lower than in the Atlantic.

Silicate

Silicon (Si) was born in the universe by fusion between atoms of oxygen (O). It is the seventh most abundant element in the universe, the second most abundant in the Earths crust. Weathering (dissolution) of silicate rocks and minerals at low or high temperatures generates silicic acid (H_4SiO_4 or $Si(OH)_4$), so-called dissolved silica (DSi). Discharge of rivers and of submarine groundwater into the coastal ocean, hydrothermal inputs into deep waters, dissolution of siliceous material transported from the continents to the continental margins and that of air-borne suspended materials in surface waters are pathways for DSi input into the ocean. In surface waters, DSi is taken up by diatoms to build their frustules of amorphous biogenic silica (bSiO2). Removal of DSi from the ocean corresponds mostly to the burial of biogenic silica, as opal, in abyssal and coastal sediments, although a minor contribution from siliceous sponges might also be involved. A budget of Si in the world ocean (Figure 2.6) has been published by *Tréguer and De La Rocha* (2013).

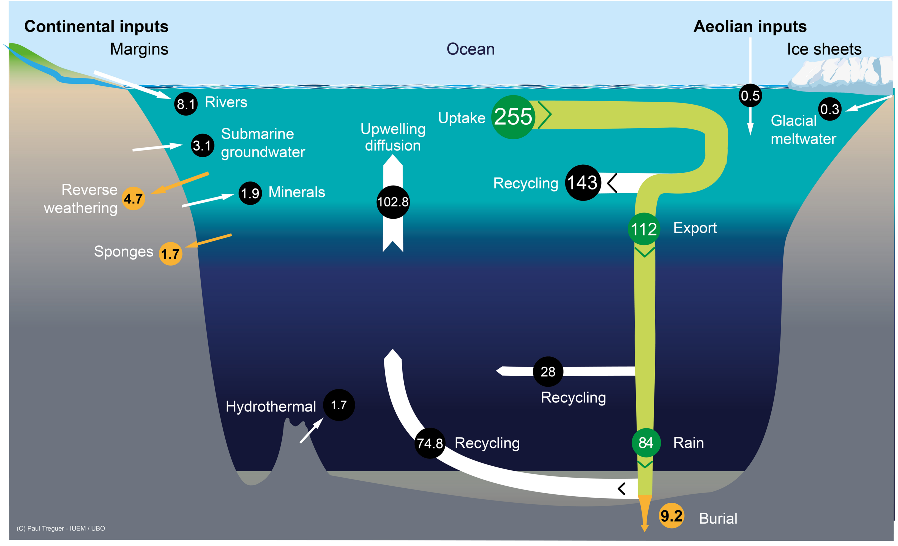

Figure 2.6: The Si cycle in the modern world ocean includes the input, output, and biological Si fluxes. The white arrows represent fluxes of net sources and recycled of DSi. Orange arrows correspond to sink fluxes of Si (either as biogenic silica or as authigenic silica). Green arrows correspond to biological (pelagic) fluxes. All fluxes are in teramoles of silicon per year (Tmol Si yr^{-1}). Figure source: Tréguer et al. (2021).

The key role played by the Southern Ocean in the control of the world ocean silica cycle was identified long ago (e.g., *Anderson et al.* (2002); *DeMaster* (1981, 2002); *Nelson et al.* (1995); *Pondaven et al.* (2000); *Tréguer et al.* (1995)). At subsurface and intermediate depths, SAMW and AAIW export huge amounts of DSi that remains unused by siliceous phytoplankton in Southern Ocean surface waters. In the abyss, DSi-rich AABW also exports DSi into the deep areas of the Atlantic, Indian, and Pacific basins (*Anderson et al.*, 2002). On the other hand, the large opal belt of opaline sediments that girds the Antarctic, roughly underlying the Polar Frontal Zone, has been cored for several decades (e.g., *DeMaster* (1981, 2002)). The impressive abundance of biogenic silica in the opal belt sediments makes the Southern Ocean one of the most important silica sinks in the world ocean (*DeMaster*, 2002; *Pondaven et al.*, 2000). However, *Tréguer* (2014) stated that the Southern Ocean is a net receiver of DSi. At the steady state, the Southern Ocean imports 2.0(±1.2) teramoles of silicon per year, via the CDW.

2.2.4 The Southern Ocean Biogeochemical Divide

Marinov et al. (2006) first identified the SOBD and demonstrated its importance in controlling nutrient and carbon distribution, as well as its impact on global climate. This divide is characterized by differences in nutrient levels and carbon sequestration efficiency between the Antarctic and Subantarctic regions of the Southern Ocean. The SOBD is a conceptual line within the Southern Ocean that separates regions of different biological activity and chemical properties in the water. To the south of the SOBD (the lower cell), limited nutrient utilization by phytoplankton leads to unutilized nutrients and CO_2 being sequestered in the deep ocean through deep water formation processes. In contrast, to the north of the SOBD (the upper cell), increased nutrient utilization, potentially driven by increased iron availability, results in partial consumption of nutrients before they are subducted to form intermediate and mode waters.

Nutrient utilization by phytoplankton in different regions of the Southern Ocean significantly impacts the marine carbon and nutrient cycles (*Marinov et al.*, 2006; *Oschlies et al.*, 2010; *Primeau et al.*, 2013). The region south of the SOBD are more critical for atmospheric CO_2 regulation than the region to the north. In this southern region, limited phytoplankton activity results in minimal nutrient utilization, allowing unutilized nutrients and CO_2 to sink with the AABW and remain sequestered in the abyss for centuries to millennia until being re-exposed to the surface. This process effectively reduces atmospheric CO_2 levels. Conversely, in the upper cell, increased nutrient utilization, potentially driven by increased iron availability, results in partial consumption of nutrients before they are subducted with AAIW and SAMW, maintaining a relatively shallow cycle that contributes to primary production outside the Southern Ocean (*Hauck et al.*, 2018; *Sarmiento et al.*, 2004). Thus, upper cell primary production in the Southern Ocean competes with downstream primary production outside the Southern Ocean for nutrients. For example, if more upper cell nutrients are utilized, downstream production will be reduced (*Holzer and Primeau*, 2013; *Marinov et al.*, 2006; *Primeau et al.*, 2013). Indeed, model simulations suggest that as much as 75% of marine primary production north of 30°S is fueled by nutrients supplied by AAIW and SAMW (*Sarmiento et al.*, 2004).

The relevance of the SOBD for the marine nutrient and carbon cycle has been assessed by BGC modeling (*Holzer et al.*, 2014; *Marinov et al.*, 2006; *Primeau et al.*, 2013). *Marinov et al.* (2006)'s findings using the Geophysical Fluid Dynamics Laboratory Modular Ocean Model version 3 (MOM3) coupled with an Ocean Carbon Cycle Model Intercomparison Project (OCMIP) 2 biogeochemistry model revealed several insights into the SOBD. They identified it as a distinct BGC boundary between the Antarctic and Subantarctic regions—referred to as the SOBD—which leads to a significant division in nutrient concentrations and biological productivity. Their findings emphasized that nutrient depletion in the Antarctic leads to increased nutrient availability and productivity at intermediate and subtropical latitudes, while Subantarctic depletion has a more significant local effect but a smaller global impact. The study also concluded that the efficiency of the biological carbon pump in the Southern Ocean plays a critical role in atmospheric CO_2 levels, and regional differences in nutrient sequestration efficiency should be considered in global BGC models.

Recent studies have identified the SOBD's location. A physical oceanography study has identified the surface boundary between the upper and lower overturning cells based on the MOC. *Pellichero et al.* (2018) explored the MOC in the Southern Ocean in a water mass transformation framework using observations and identified the neutral density $\gamma = 27.6 \mathrm{kg}/\mathrm{m}^3$ outcrop as the dividing line between the upper and lower cells. *Xie et al.* (2022) approached the challenge of localizing the SOBD through a methodological framework involving the high-resolution Australian Community Climate and Earth System Simulator (ACCESS-OM2-01) ocean-sea ice model and particle tracking through the Connectivity Modeling System (CMS) to simulate and analyze the SOBD. The study found that the SOBD is not a static feature but is influenced by a complex interplay of oceanographic factors, suggested that the SOBD is a wide circumpolar band that varies depending on several factors, including Ekman transport, the ACC, subpolar gyre circulation, and surface buoyancy fluxes.

Chapter 3

Data and Methods

3.1 Data

The data used in this thesis were model output from the Norwegian Earth System Model Version 2 (NorESM2) and mapped data from the World Ocean Atlas 2018 (WOA18).

3.1.1 The Norwegian Earth System Model Version 2

For this thesis, the NorESM2-MM model configuration of NorESM2 is employed. NorESM2-MM is a fully coupled model configuration, integrating multiple components of the Earth's climate system, including the atmosphere, ocean, sea ice, land surface, and BGC cycles. It is forced by greenhouse gas concentrations (climate models are usually configured with either concentration-driven or emission-driven forcing fields), the prescribed CMIP6 solar forcing (see *Matthes et al.* (2017)) and aerosol emissions. The physical parameters are configured according to *Seland et al.* (2020), and *Tjiputra et al.* (2020) for configurations and parameterizations specific to ocean BGC. Model output is stored in the ESGF archive, which contains homogenized and standardized outputs (including variable names). More specifically, all data is in compliance with the standards of the Climate Model Output Rewriter (CMOR) (*NorESM2*, 2020). The data is accessed through the (Norwegian) National Infrastructure for Research Data (NIRD), which hosts the CMOR-ized CMIP6 data provided by NorESM2. The dataset includes historical data spanning from 1850 to 2014.

NorESM2 is the second generation of the coupled Earth system model (ESM) developed by the Norwegian Climate Center, succeeding NorESM1 (*Bentsen et al.*, 2013; *Iversen et al.*, 2013; *Kirkevåg et al.*, 2013; *Tjiputra et al.*, 2013). NorESM2 is based on the Community Earth System Model (CESM) 2.1 (*Danabasoglu et al.*, 2020). Although large parts of NorESM are similar to CESM, there are several important differences. NorESM uses the Bergen Layered Ocean Model (BLOM) and the isopycnic coordinate Hamburg Ocean Carbon Cycle (iHAMOCC) model for ocean biogeochemistry (*Tjiputra et al.*, 2020). It also utilizes a different atmospheric aerosol module (*Kirkevåg et al.*, 2018). It features specific modifications and tunings of the physics and dynamics of the atmosphere component (*Toniazzo et al.*, 2020).

NorESM2 contributes to the 6th phase of the Coupled Model Intercomparison Project (CMIP6) (*Eyring et al.*, 2016), assessing pre-industrial climate stability, the model's response to abrupt and gradual CO_2 quadrupling, and its ability to simulate historical climate under CMIP6 forcing. It is an improvement over its predecessors in most respects, with a less sensitive response to greenhouse gas forcing and an estimated equilibrium climate sensitivity of 2.5 K over a 150-year timeframe (*Seland et al.*, 2020).

NorESM2 is available in three configurations (*Seland et al.*, 2020):

- **NorESM2-MM:** 1-degree resolution for all model components (We use this configuration for the study)
- **NorESM2-LM:** 2-degree resolution for the atmosphere and land components; 1-degree resolution for the ocean and sea-ice components; emission-driven mode for CO_2 concentration (default)
- **NorESM2-MH:** 1-degree resolution for the atmosphere and land components; 0.25-degree resolution for the ocean and sea-ice components (This configuration has not been used for long historical simulations)

We use the data from NorESM2-MM model output from the ocean biogeochemistry component, iHAMOCC, in NorESM2. The iHAMOCC prognostically simulates five key ocean BGC cycle processes (*Tjiputra et al.*, 2020):

- **Inorganic Seawater Carbon Chemistry:** iHAMOCC's carbon chemistry formulation is based on OCMIP protocols. It computes the pCO_2 in the surface layer using temperature, salinity, dissolved inorganic carbon, and alkalinity concentrations. The pCO_2 value is used to estimate air-sea CO_2 fluxes. In addition to surface pCO_2, the water column pH, carbonate ion, and calcite saturation state are all calculated.
- **NPZD-type Ecosystem Module:** In the euphotic layer of the model (top 100 m), the lower trophic ecosystem dynamic is simulated using an NPZD (Nutrient Phytoplankton Zooplankton Detritus) ecosystem module (*Six and Maier-Reimer*, 1996). One phytoplankton and one zooplankton bulk compartments are simulated together with multiple limiting nutrients (NO_3, PO_4, and dissolved iron), dissolved organic carbon and particulate matter. In addition to nutrients, the primary production is also limited by light availability and temperature. A fixed stoichiometry Redfield Ratio is used to govern the fluxes of nutrients and carbon among the different ecosystem compartments.
- **Air-sea Gas Exchange:** The air-sea gas exchange formulation by *Wanninkhof* (2014) to compute fluxes of CO_2, O_2, DMS (Dimethyl Sulfide), N_2, N_2O, CFC-11, CFC-12, and SF_6 gases. These fluxes are computed as a function of surface wind speed, Schmidt number, gas solubility, and partial pressure difference of the respective gases. For DMS, the flux is always from the ocean to the atmosphere.
- **Vertical Fluxes of Inorganic and Organic Particles:** Biological activity in the upper ocean produces particulate matter that is transported vertically and remineralized in the water column (*Schwinger et al.*, 2016). For particulate organic carbon, the sinking speed is increased with depth, while a constant remineralization rate is used throughout the water column. For biogenic silica (opal), both a

constant vertical sinking speed and a dissolution rate are used. For particulate inorganic carbon ($CaCO_3$), a constant sinking speed is used while the dissolution is formulated as a function of calcite saturation state.

- **Sediment Biogeochemistry:** A 12-layer sediment module is included in iHAMOCC (*Heinze et al.*, 1999). It collects the sinking particle matters that are not completely dissolved or remineralized in the water column. It includes four solid sediment components ($CaCO_3$, opal, organic carbon, and clay), and five pore water substances (dissolved inorganic carbon, alkalinity, PO_4, oxygen, and silicate). In addition to particle deposition, it simulates fluxes of tracers with the bottom-most ocean layer through pore water chemistry and diffusion.

3.1.2 Observational Data

This thesis makes use of the WOA18, which provides detailed climatologies of the world's ocean properties, to validate the output of the NorESM2 simulations. This validation process helps to assess the accuracy of the model simulations in replicating observed oceanic conditions, such as temperature, salinity, nutrient concentrations, and DO levels. We can identify discrepancies and validate the model's capability to simulate various oceanic processes and dynamics accurately by comparing the model outputs against these well-established observational datasets. The WOA18 helps us understand both biochemical processes like marine production and respiration, as well as physical processes like advection and water mass renewal. We conducted our analysis using data on dissolved inorganic nutrients (PO_4 and Si) and DO. The atlas contains a systematic, objective analysis of historical oceanographic profiles obtained from instruments such as rosette CTD packages. These profiles serve as the foundation for climatologies, which are defined as mean oceanographic fields at specific standard depth levels. This data ranges from the ocean's surface to a maximum depth of 5500m. Each parameter studied—PO_4, Si, and DO—is represented by a consistent, objective one-degree latitude-longitude grid (*Garcia et al.*, 2019a,b).

Dissolved Inorganic Nutrients (Phosphate and Silicate)

Biochemical processes influence the global distribution and concentration of dissolved inorganic nutrients in the ocean, such as marine production, respiration, and the breakdown of organic matter, as well as physical processes, including water mass renewal, advection, and mixing. The term "nutrients" in this atlas refers specifically to chemically reactive dissolved inorganic ortho-PO_4 or PO_4, as well as ortho-silicic acid or Si. These measurements are expressed in units of micro-mole per kilogram (μmol/kg). All nutrient climatologies make use of all available quality controlled data, regardless of the year of observation. The data used in this atlas were collected from 1960 to 2017. The annual climatology was calculated using all data, regardless of the month in which the observation occurred (*Garcia et al.*, 2019b).

Dissolved Oxygen

WOA18 selects annual climatologies and related statistical fields for DO, apparent O_2 utilization (AOU), and O_2 saturation ($S\ O_2$). Biochemical and physical processes influence the ocean's DO distribution, AOU, and S O_2. BGC processes include DO sources and sinks caused by marine production, respiration, and organic matter oxidation (for example, biological pumps). Water mass ventilation, air-sea flux exchange, gas solubility (e.g., thermal pump), and water mixing are all examples of physical processes that affect O_2. The oceanic DO inventory is sensitive to local to global changes caused by the physical and biological state of the ocean, as well as anthropogenic effects on various time and spatial scales. This atlas provides a comprehensive overview of data analysis procedures and horizontal maps that display annual climatologies and associated statistical fields. All climatologies utilize all DO data collected from 1960 to 2017. The annual climatology was computed by considering all data, irrespective of the month of observation (*Garcia et al.*, 2019a).

3.2 Methods

We consider physical parameters to help us with our main BGC analysis. Then, we illustrate all the methods we use for our main analysis: to see the distributions of the BGC tracers in the Southern Ocean; time series analysis; and the SOBD location. All data was processed in Python.

3.2.1 Detect Depth Level for Isopycnal Outcropping

We do density analysis to help decide the depth level that we will examine to do the time series analysis. Figure 3.1 shows isopycnals in latitude-depth transects for three sectors (Atlantic, Pacific, and Indian Ocean) in the Southern Ocean from NorESM2-MM, analyzed over a 10-year span from 2000–2009. For each ocean, the isopynals at intermediate depth lie in between 1036–1037 $\mathrm{kg/m^3}$. To check which isopynal and depth could be suitable to represent the SOBD along with BGC output, we plotted the latitude of crossing points at 1036, 1036.5, and 1037 $\mathrm{kg/m^3}$ density levels and 100m, 250m, and 500m depth over time and selected data along the longitudes of 25.5°W (Atlantic Sector), 150.5°W (Pacific Sector), and 90.5°E (Indian Sector) and restricted between 30°S and 90°S. As we expect the core of the upwelling region to be more stable than the periphery, we look to associate the SOBD with an isopynal for which the depth crossing point has relatively small latitudinal fluctuations. As the plot shows in Figure 3.2, density at 1036.5 $\mathrm{kg/m^3}$ has less fluctuation throughout the depth. For the depth condition, we would like it to be close to the surface but avoid effects originating from the surface mixed layer; 250m is a suitable depth. To confirm that at 250m depth, the isopynal 1036.5 $\mathrm{kg/m^3}$ doesn't get much surface/seasonal effects over time, we plotted the isopycnal outcropping over time from 1850–2014 (same time span for the time series analysis that we will perform later) for the three ocean sectors. The outcomes from Figure 3.3 show that at this isopycnal and the depth, the water column is not strongly influenced by surface/seasonal effects. This information helps us with other analyses for detecting the SOBD location, which we will describe further in the methods section.

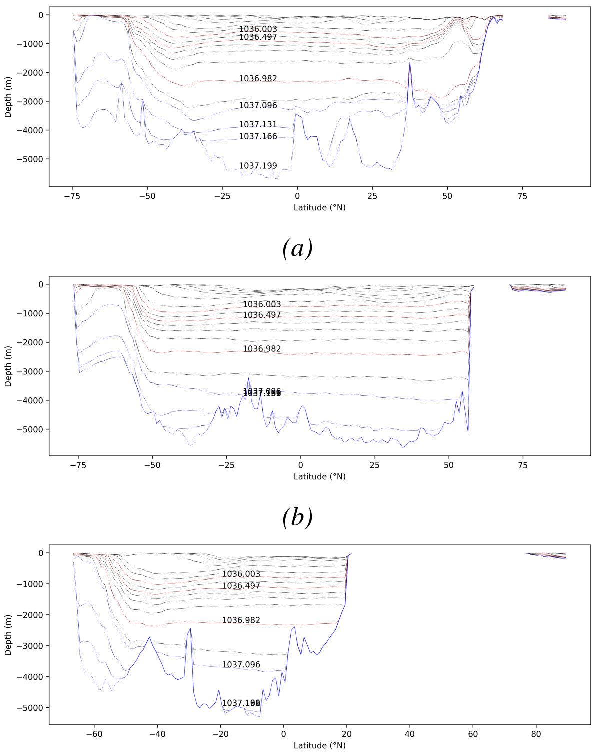

(a)

(b)

(c)

Figure 3.1: Isopycnal in latitude-depth transects in (a) Atlantic, (b) Pacific, and (c) Indian Sectors. Data from NorESM2-MM historical simulations from 2000–2009

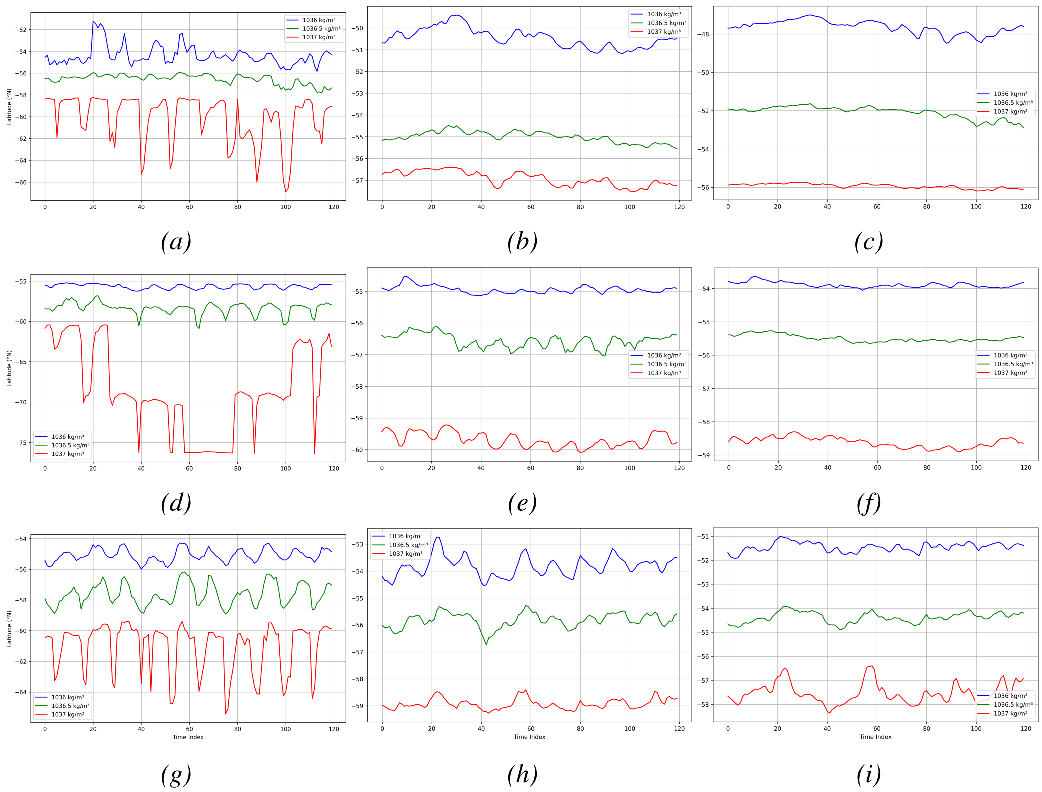

(a) *(b)* *(c)*

(d) *(e)* *(f)*

(g) *(h)* *(i)*

Figure 3.2: Latitude of 100m (a,d,g), 250m (b,e,h), and 500m (c,f,i) Depth Crossing for 1036 (blue), 1036.5 (green), and 1037 (red) $\mathrm{kg/m^3}$ *over 10 years span in (a–c) Atlantic, (d–f) Pacific, and (g–i) Indian Sectors. Data from NorESM2-MM historical simulations.*

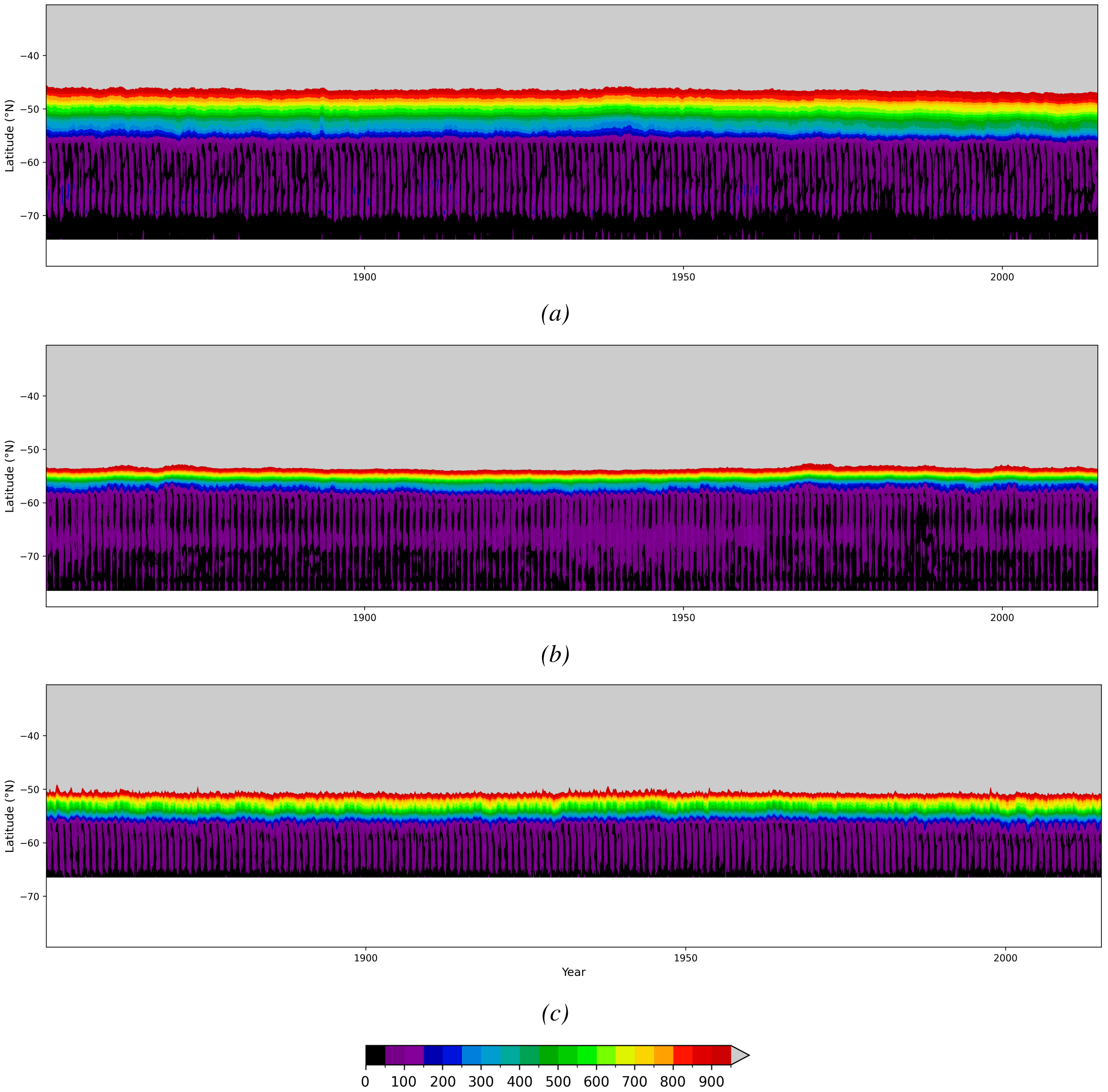

(a)

(b)

(c)

Figure 3.3: Latitude plot of 1036.5 $\mathrm{kg/m^3}$ *isopycnal depth outcropping over time from 1850–2014 in (a) Atlantic, (b) Pacific, and (c) Indian Sectors. Data from NorESM2-MM historical simulations.*

3.2.2 Distributions of Biogeochemical Tracers in the Southern Ocean

We have used dataset analysis outputs from the NorESM2-MM and the WOA18 to examine how PO_4, DO, and Si were distributed in the Southern Ocean. The analysis was carried out in two main formats: South Polar Stereographic projections for surface and 250m depth visualization and latitude-depth transects for vertical distribution assessment. The objective is to compare the model output with the observation data to see how well NorESM2-MM performs. NorESM2-MM provides historical simulation output data from 1850 to 2014, and WOA18 provides the tracers' annual data in netCDF from 1900 to 2017. For suitable comparison outcomes, we chose the data span from 1900 to 2014 for NorESM2-MM.

NorESM2-MM

South Polar Stereographic projection maps

- Load netCDF datasets containing concentrations of PO_4, DO, and Si (the tracers) spanning from 1900 to 2014 on a 1-degree grid.
- Select data at the surface level and at 250m (our selected depth to detect the SOBD).
- Compute the average concentrations of the tracers over the time dimension to provide an overview of their distribution throughout the dataset's timeline.
- Convert the tracers' concentrations from mol/L to μmol/L by multiplying by 1000.
- Initialize a plotting area with a South Polar Stereographic projection, setting latitude limits from -90 to -30 °N to cover the Antarctic region and longitude limits from -180 to 180 degrees to encompass all global longitudes.

Latitude-depth transects

- Load netCDF datasets containing concentrations of PO_4, DO, and Si (the tracers) spanning from 1900 to 2014 on a 1-degree grid.
- Use xESMF to regrid data onto a regular latitude-longitude grid with a resolution of 1 degree.
- Average the data over time.
- Select data along the longitudes of 25.5°W (Atlantic Sector), 150.5°W (Pacific Sector), and 90.5°E (Indian Sector).
- Convert the tracers' concentrations from mol/L to μmol/L by multiplying by 1000.
- Select depths ranging from the surface to the bottom (0–5500m).

WOA18

South Polar Stereographic Projection maps

- Load netCDF datasets containing annual concentrations of PO_4, DO, and Si (the tracers) on a 1-degree grid from 1900 to 2017. These datasets do not contain time variables.
- Utilize objectively analyzed mean fields for the molar concentration of the tracers in seawater at standard depth levels for this analysis.
- Select data at the surface level and at 250m (our selected depth to detect the SOBD).
- Convert the tracers' data from μmol/kg to μmol/L by multiplying by the density (kg/m^3) dataset to align with the model data.
- Initialize a plotting area with a South Polar Stereographic projection, setting latitude limits from -90 to -30 °N to cover the Antarctic region and longitude limits from -180 to 180 degrees to encompass all global longitudes.

As these are observation dates, Figure 3.4 shows the number of observations of the tracers in each grid square at each depth level.

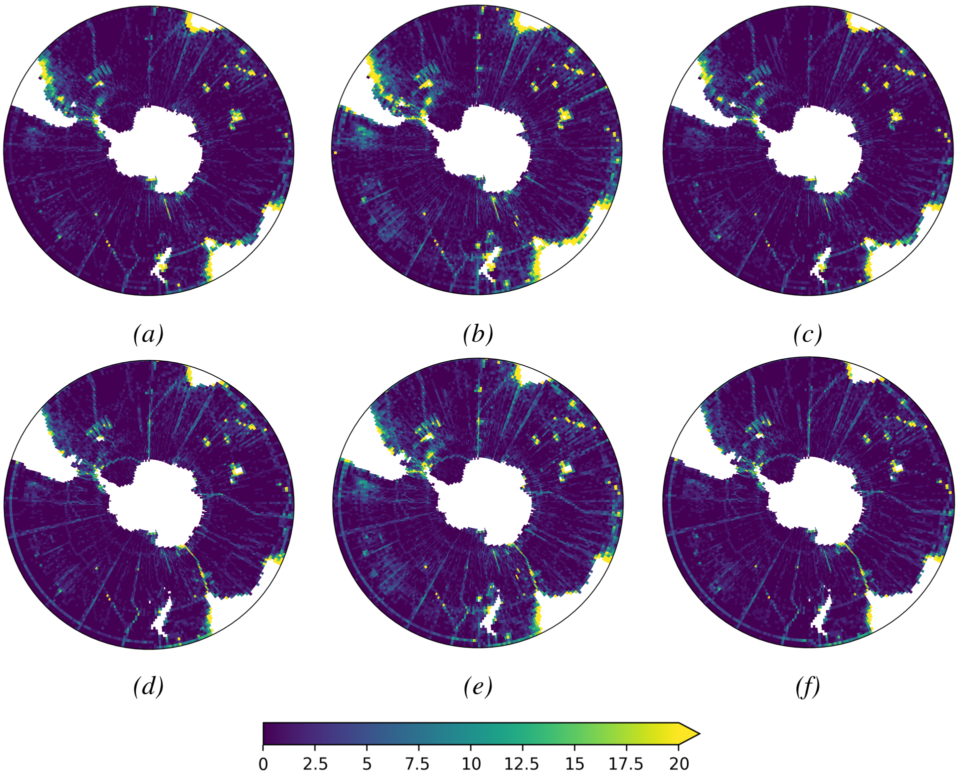

Figure 3.4: The number of observations of PO_4 *(a,d), DO (b,e), and Si (c,f) in each grid square at the surface (a–c) and 250m (d–f) depth level.*

Latitude-Depth transects

- Load netCDF datasets containing annual concentrations of PO_4, DO, and Si (the tracers) on a 1-degree grid from 1900 to 2017. These datasets do not contain time variables.
- Utilize objectively analyzed mean fields for the molar concentration of the tracers in seawater at standard depth levels for this analysis.
- Select data along the longitudes of 25.5°W (Atlantic Sector), 150.5°W (Pacific Sector), and 90.5°E (Indian Sector).
- Convert the tracers' data from μmol/kg to μmol/L by multiplying by the density ($\mathrm{kg/m^3}$) dataset to align with the model data.
- Select depths ranging from the surface to the bottom (0–5500m).

As there are observation dates, Figure 3.5 shows the number of observations of the tracers in each grid square at each standard depth of each sector.

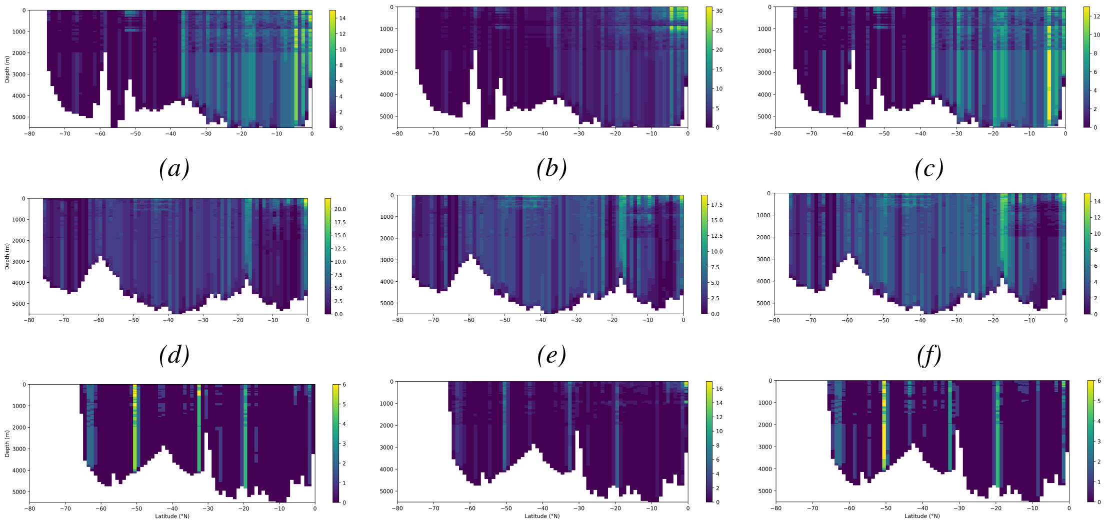

(a) *(b)* *(c)*

(d) *(e)* *(f)*

(g) *(h)* *(i)*

Figure 3.5: The number of observations of PO_4 *(a,d,g), DO (b,e,h), and Si (c,f,i) in each grid square at each standard depth of Atlantic (a–c), Pacific (d–f), and Indian (g–i) Sectors.*

3.2.3 Time Series Analysis

These analyses focus on the time series analysis of the BGC tracers in three sectors in the Southern Ocean. All time series analyses using NorESM2-MM (1-degree grid) historical simulation output data in all time spans available (1850–2014).

Tracers Concentrations

- Load netCDF datasets containing concentrations of PO_4, DO, and Si (the tracers) from the model.
- Use xESMF to regrid data onto a regular latitude-longitude grid with a resolution of 1 degree.

- Select data along the longitudes of 25.5°W (Atlantic Sector), 150.5°W (Pacific Sector), and 90.5°E (Indian Sector).
- Select data at the surface, 100m, and 250m depth levels.
- Set latitude limits from -76.5 to -30.5 °N, covering the Southern Ocean.
- Convert the tracers' data from mol/L to μmol/L.
- Plot time series analysis of the tracers' concentrations across latitudes.

Tracers Anomalies

- Load netCDF datasets containing concentrations of PO_4, DO, and Si (the tracers) from the model.
- Use xESMF to regrid data onto a regular latitude-longitude grid with a resolution of 1 degree.
- Select data along the longitudes of 25.5°W (Atlantic Sector), 150.5°W (Pacific Sector), and 90.5°E (Indian Sector).
- Select data at the surface, 100m, and 250m depth levels.
- Set latitude limits from -76.5 to -30.5 °N, covering the Southern Ocean.
- The latitude limits are set from -76.5 to -30.5 °N, covering the Southern Ocean.
- Compute the annual mean, reducing the time dimension to yearly averages.
- Compute tracers anomalies by subtracting the long-term mean from the annual means.
- Convert the tracers' data from mol/L to μmol/L.
- Plot time series analysis of the tracers anomalies across latitudes.

Seasonal Effect

- Load netCDF datasets containing concentrations of PO_4, DO, and Si (the tracers) from the model.
- Use xESMF to regrid data onto a regular latitude-longitude grid with a resolution of 1 degree.
- Select data along the longitudes of 25.5°W (Atlantic Sector), 150.5°W (Pacific Sector), and 90.5°E (Indian Sector).
- Select data at the surface, 100m, and 250m depth levels.
- Set latitude limits from -76.5 to -30.5 °N, covering the Southern Ocean.
- The latitude limits are set from -76.5 to -30.5 °N, covering the Southern Ocean.

- Calculate the monthly mean for each year, creating a new dataset of average tracers concentrations for each month.
- Convert the tracers' data from mol/L to μmol/L.
- Plot time series analysis of the tracers' concentrations across latitudes.

3.2.4 The Southern Ocean Biogeochemical Divide Location

As we explain in 3.2.1, we would like to represent the BGC outputs in alignment with the physical output. Our identical SOBD location is computed as follows:

- Load netCDF datasets containing concentrations of PO_4, DO, Si (the tracers), and density from the model.
- Use xESMF to regrid data onto a regular latitude-longitude grid with a resolution of 1 degree.
- Select data at 250m depth (our selected depth to detect the SOBD).
- Average the tracers and density data over time, selecting the density value closest to 1036.5 kg/m^3 for the isopycnal layer.
- Initialize a plotting area with a South Polar Stereographic projection, setting latitude limits from -90 to -45 °N to cover the Antarctic region and longitude limits from -180 to 180 degrees to encompass all global longitudes.
- Convert the tracers' data from mol/L to μmol/L.
- Plot the tracers' concentrations across the region and the isopycnal line at 1036.5 kg/m^3.
- Use orsifronts package in R to plot the locations of the PF, SB of ACC and SACCF.

Chapter 4

Results and Discussion

4.1 Distributions of Biogeochemical Tracers in the Southern Ocean

Figure 4.1 shows the annual mean distribution of BGC tracers (PO_4, DO, and Si) in the Southern Ocean, based on NorESM2-MM data. PO_4 concentrations are around 1.5 μmol/L at the surface, and at a depth of 250m, the concentrations reach maximum values of 1.9 μmol/L. At both depths, around 50°S, there is a gradual decrease in PO_4 concentrations moving northwards towards lower latitudes. DO at the surface shows the highest concentrations, approximately 360 μmol/L, close to the Antarctic continent. At a depth of 250m, the highest DO concentrations are still observed near the continent, although the overall DO concentration at this depth is lower than at the surface. The distribution pattern of Si in the Southern Ocean is similar to that of PO_4 but with higher concentrations, ranging from around 45 μmol/L to a maximum of approximately 60 μmol/L. At 250m depth, Si concentrations are higher than those at the surface.

The latitude-depth transects of the tracers with isopynal across three sectors of the Southern Ocean are shown in Figure 4.2. These transects provide a more detailed view of the tracer distribution from the surface to the deep ocean, allowing us to identify the water masses in each ocean. Characteristics of high nutrients but low DO in CDW are evident in all three oceans. At a depth of 500m, CDW is located near 50°S in the Atlantic, close to 55°S in the Pacific, and around 57°S in the Indian Ocean. The NorESM2-MM model data shows: AABW, characterized by high nutrients and DO; AAIW, found at an intermediate depth of approximately 500–1,000m with relatively high DO and intermediate nutrient levels compared with overall; and SAMW, which has high DO and relatively low nutrients. South of 45°S, the pattern of the tracers in each ocean compared with each other does not show significant different pattern. However, north of 45°S, the Pacific exhibits the highest PO_4 concentrations (more than 3 μmol/L, from approximately 25°S to the equator, at depths from about 500–3000m) and a broad distribution from a few hundred meters to the bottom. The Indian Ocean shows a similar distribution but with lower concentrations. Conversely, in the Atlantic, below 1200m PO_4 values are relatively low compared to the other two oceans. For Si, the distributions are similar to those of PO_4 but with high concentrations at the bottom of each ocean. The Pacific also shows maximum values exceeding 160 μmol/L

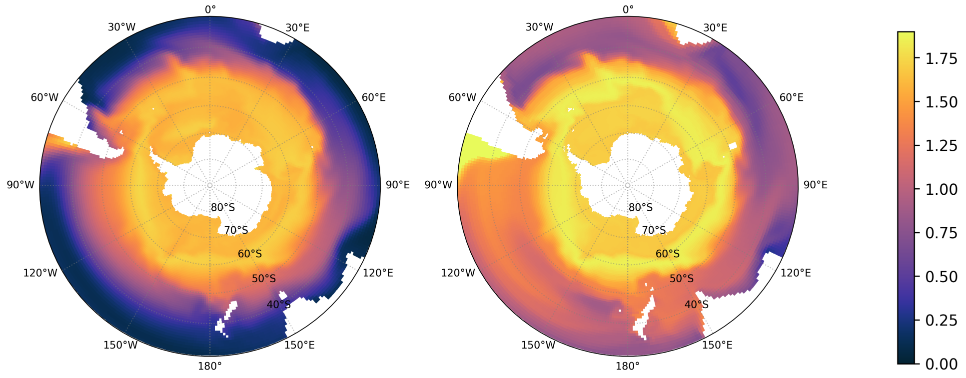

(a) PO_4, surface (b) PO_4, 250m depth

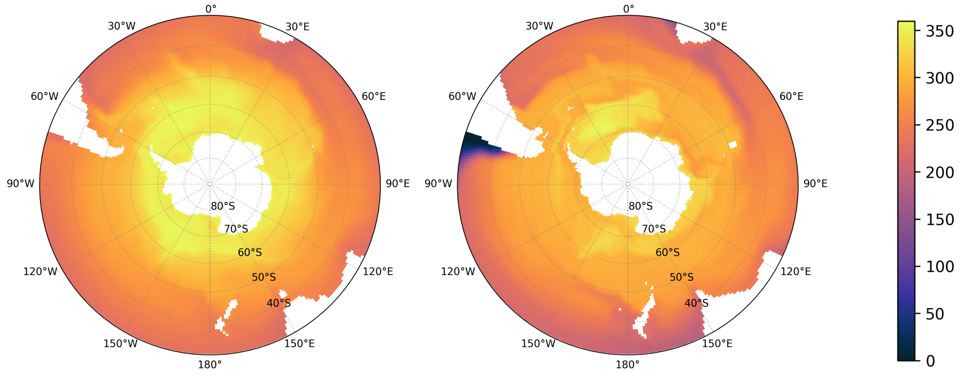

(c) DO, surface (d) DO, 250m depth

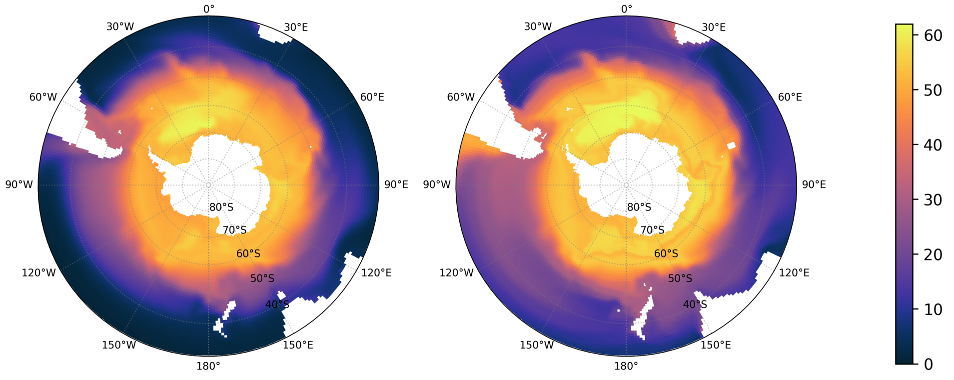

(e) Si, surface (f) Si, 250m depth

Figure 4.1: Mean concentrations of (a,b) PO_4, (c,d) DO, and (e,f) Si (μmol/L) in the Southern Ocean. (a,c,e) show surface data and (b,d,f) at 250m depth. Data from NorESM2-MM historical simulations (1900–2014). Visualizations are projected using a South Polar Stereographic projection encompassing latitudes from 30°S to 90°S.

(from around 25°S to the equator, at depths from about 2000–3500m). From 45°S northwards, DO concentrations (Figure 4.2d–f) show an inverse relationship with PO_4 concentrations, with oxygen minimum zones occurring where PO_4 concentrations are high.

In Figures 4.3–4.8, we compared the distributions of the tracers from the NorESM2-MM (1900–2014) and WOA18 observations (1900–2017) data. Nutrient concentrations in the Southern Ocean, as modeled by NorESM2-MM, tend to underestimate the actual values. For PO_4 (Figure 4.3), WOA18 shows a maximum around 2 $\mu\text{mol}/\text{L}$ at the surface and more than 2.5 $\mu\text{mol}/\text{L}$ at 250m depth. However, the overall spatial patterns are consistent between both datasets, showing a gradual decrease in PO_4 concentrations moving northwards from around 50°S towards lower latitudes. For Si (Figure 4.7), WOA18 shows concentrations almost twice as high as the model data, with around 80 $\mu\text{mol}/\text{L}$ at the surface and more than 100 $\mu\text{mol}/\text{L}$ at 250m depth. Although both datasets indicate a gradual decrease in Si concentrations moving northwards, the patterns differ; WOA18 starts showing this trend around 60°S, while the NorESM2-MM data starts around 50°S. For DO (Figure 4.5), the NorESM2-MM and WOA18 show similar distribution patterns with maximum values up to 360 $\mu\text{mol}/\text{L}$ at the surface. However, they differ significantly at 250m depth. In the WOA18 data, there is a notable ring of low DO (around 250 $\mu\text{mol}/\text{L}$) surrounding the Antarctic continent.

When we compare the latitude-depth distribution of the NorESM2-MM (1900–2014) and WOA18 observations (1900–2017) data across three ocean sectors (the Atlantic, Pacific, and Indian Oceans) (Figures 4.4, 4.6, and 4.8), it appears that the model represents the concentration of tracers in AABW (in the Southern Ocean and near the bottom) differently from the observation data. The model underestimates the nutrients (PO_4 and Si) and overestimates DO in this water mass for all sectors. In the Pacific, around 25°S to the equator at depths from about 500–3000m, the model data show higher concentrations of PO_4 and Si than the WOA18 data. For Si, from around 50–20°S, assumed to be SAMW, AAIW, and CDW, the presence of these water masses seems to be deeper in the observations than in the model. For DO, the oxygen minimum zones in the NorESM2-MM show a lower concentration compared to those in the WOA18.

Analyzing the distributions of PO_4, DO, and Si together provides a clear view of the BGC processes in Southern Ocean. The surface and 250m depth distributions of the tracers exhibit consistent patterns, reflecting the influence of upwelling, nutrient-rich deep waters, and physical circulation processes. High concentrations of PO_4 and Si near the Antarctic continental margin are associated with the upwelling of CDW, which brings nutrient-rich waters to the surface. These nutrient-rich zones are crucial for supporting primary productivity in the Southern Ocean. DO concentrations are highest near the surface, especially close to Antarctica, due to atmospheric exchange and photosynthetic activity. However, the distributions at 250m depth show a decrease in oxygen levels, reflecting the utilization of oxygen for the decomposition of organic matter and upwelling of CDW.

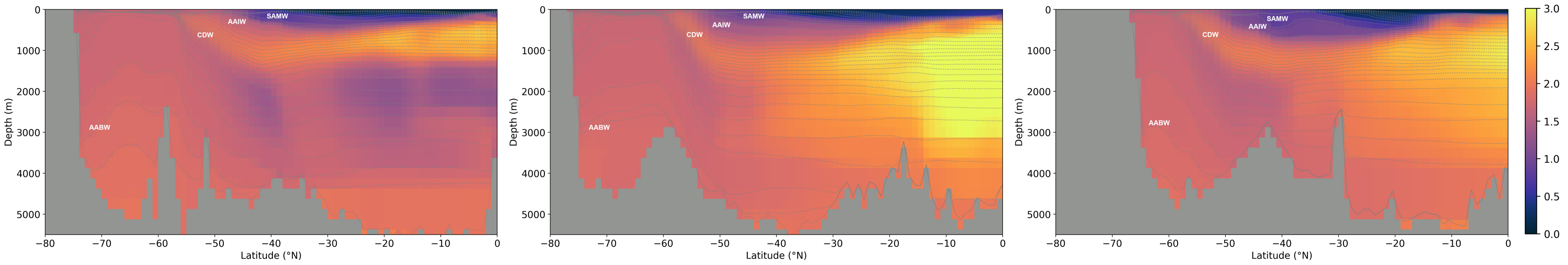

(a) PO_4, Atlantic Ocean

(b) PO_4, Pacific Ocean

(c) PO_4, Indian Ocean

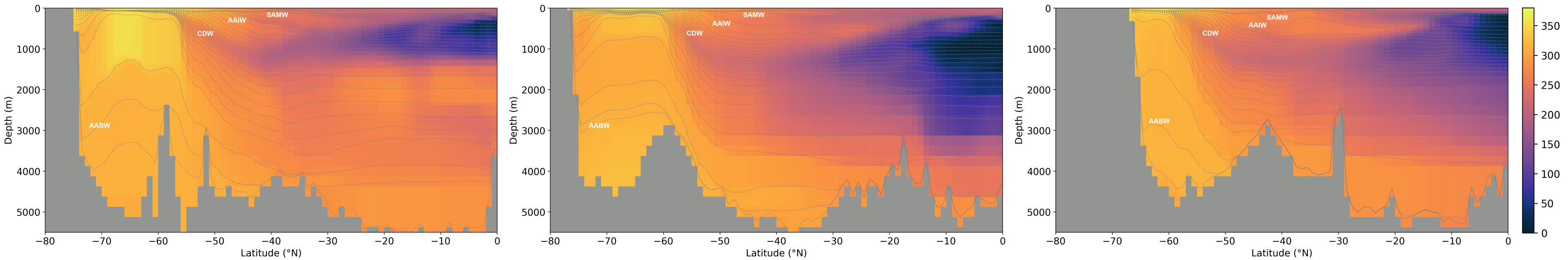

(d) DO, Atlantic Ocean

(e) DO, Pacific Ocean

(f) DO, Indian Ocean

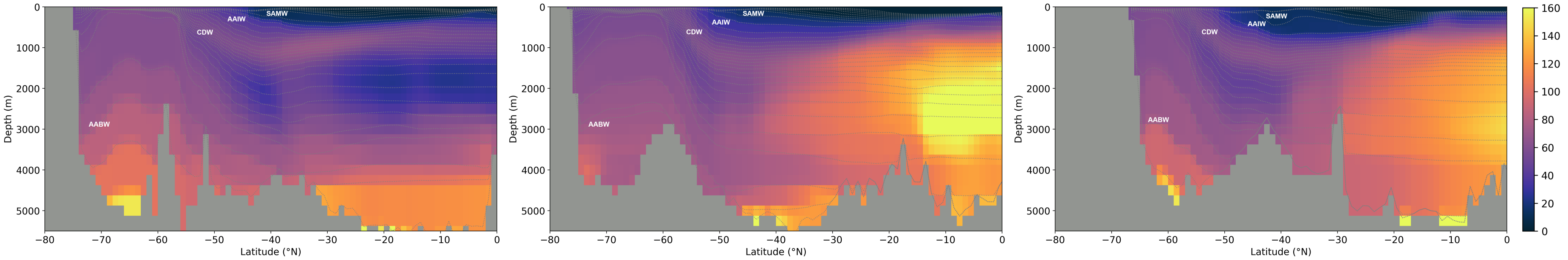

(g) Si, Atlantic Ocean

(h) Si, Pacific Ocean

(i) Si, Indian Ocean

Figure 4.2: Mean concentrations of (a–c) PO_4, (d–f) DO, and (g–i) Si (µmol/L) with isopynal in latitude-depth transects across three oceans. (a,d,g) show the Atlantic Ocean, (b,e,h) the Pacific Ocean, and (c,f,i) the Indian Ocean. Data from NorESM2-MM historical simulations (1900–2014).

The comparison of NorESM2-MM data with WOA18 observations across three ocean sectors (Atlantic, Pacific, and Indian) reveals several discrepancies. Notably, the model tends to underestimate nutrient concentrations (PO_4 and Si) and overestimate DO in the AABW. This suggests potential issues in the model's representation of deep-water formation and nutrient regeneration processes. The observed discrepancies between model outputs and observational data underscore the challenges in accurately modeling the complex BGC processes of the Southern Ocean. The underestimation of nutrient concentrations and overestimation of DO suggest that the model may not fully capture the intensity of biological production and remineralization processes.

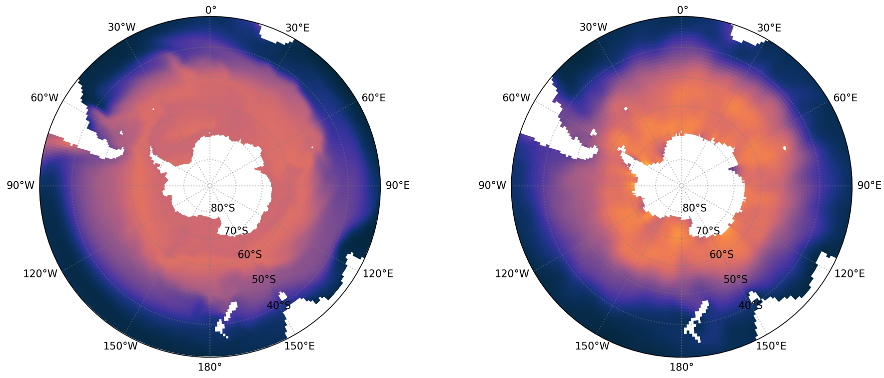

(a) NorESM2-MM, surface *(b) WOA18, surface*

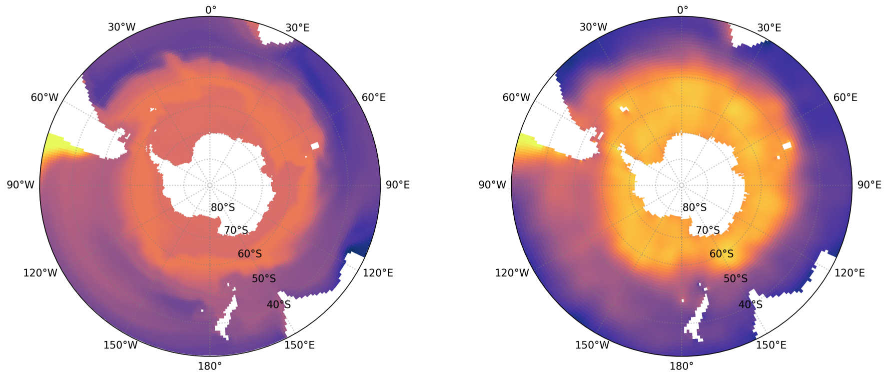

(c) NorESM2-MM, 250m depth *(d) WOA18, 250m depth*

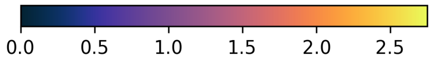

Figure 4.3: Mean concentrations of PO_4 ($\mu mol/L$) in the Southern Ocean. (a,b) show surface data and (c,d) at 250m depth. Data from NorESM2-MM historical simulations (1900–2014) in (a,c) and WOA18 observations (1900–2017) in (b,d). Visualizations are projected using a South Polar Stereographic projection encompassing latitudes from 30°S to 90°S.

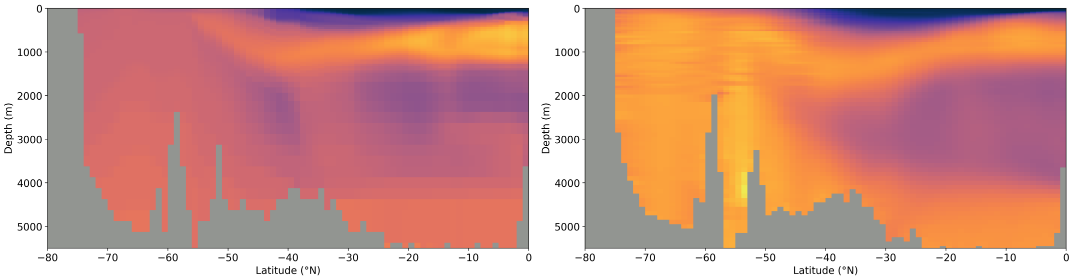

(a) *NorESM2-MM, Atlantic Ocean* (b) *WOA18, Atlantic Ocean*

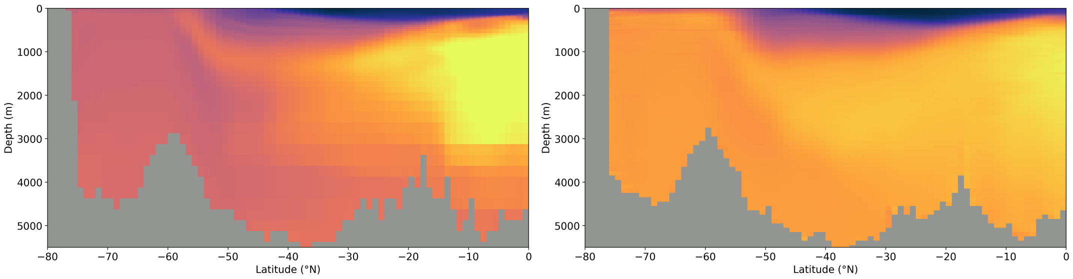

(c) *NorESM2-MM, Pacific Ocean* (d) *WOA18, Pacific Ocean*

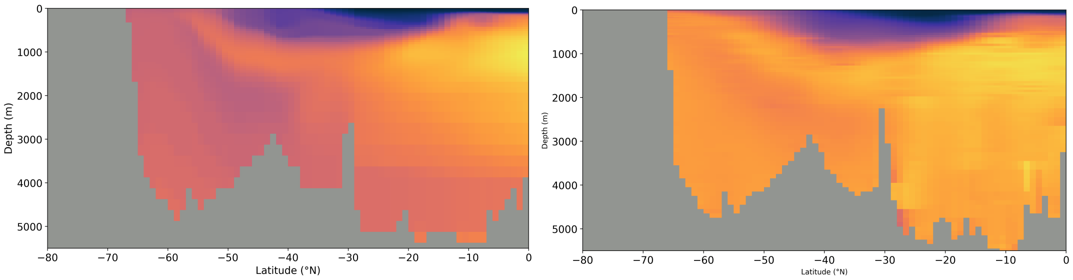

(e) *NorESM2-MM, Indian Ocean* (f) *WOA18, Indian Ocean*

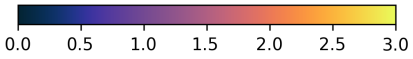

Figure 4.4: Mean concentrations of PO_4 *(*$\mu mol/L$*) in latitude-depth transects across three oceans. (a,b) represent the Atlantic Ocean, (c,d) the Pacific Ocean, and (e,f) the Indian Ocean. Data from NorESM2-MM historical simulations (1900–2014) in (a,c,e) and WOA18 observations (1900–2017) in (b,d,f).*

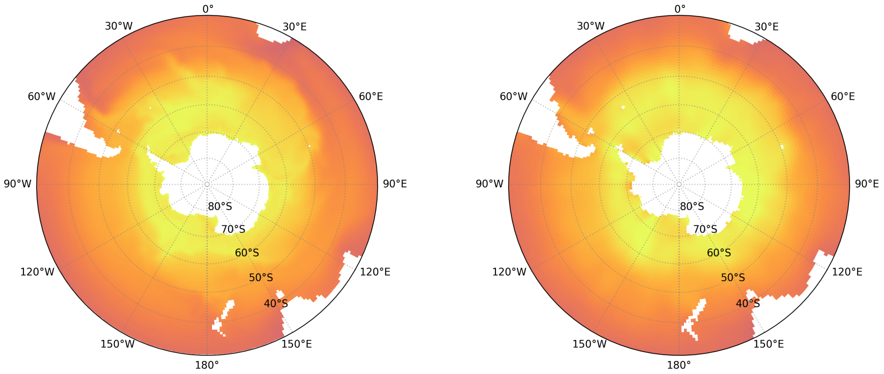

(a) NorESM2-MM, surface

(b) WOA18, surface

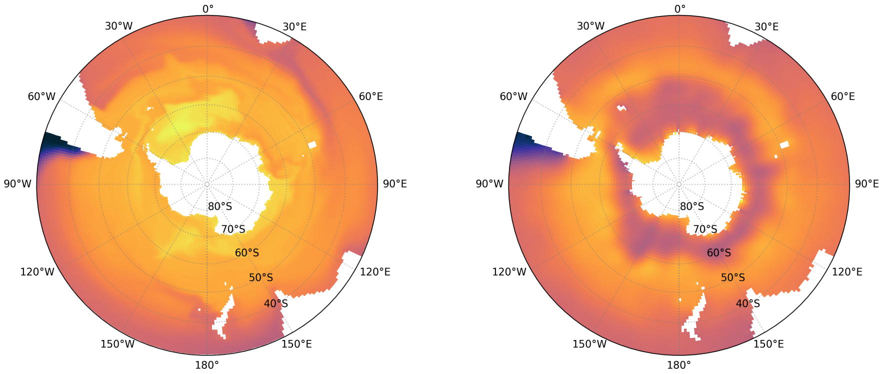

(c) NorESM2-MM, 250m depth

(d) WOA18, 250m depth

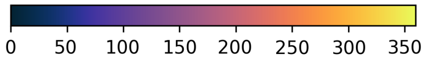

Figure 4.5: Mean concentrations of DO (µmol/L) in the Southern Ocean. (a,b) show surface data and (c,d) at 250m depth. Data from NorESM2-MM historical simulations (1900–2014) in (a,c) and WOA18 observations (1900–2017) in (b,d). Visualizations are projected using a South Polar Stereographic projection encompassing latitudes from 30°S to 90°S.

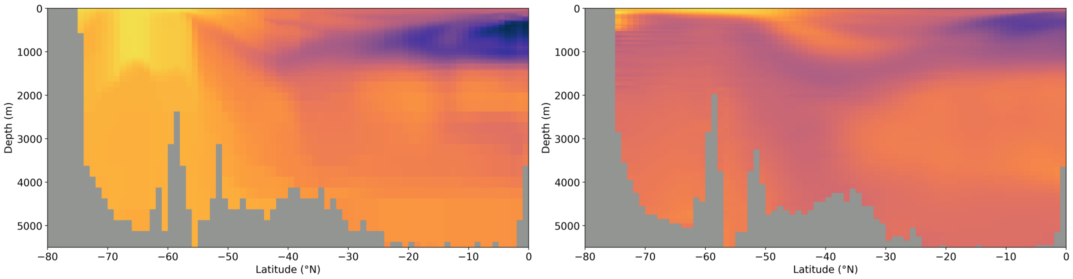

(a) NorESM2-MM, Atlantic Ocean

(b) WOA18, Atlantic Ocean

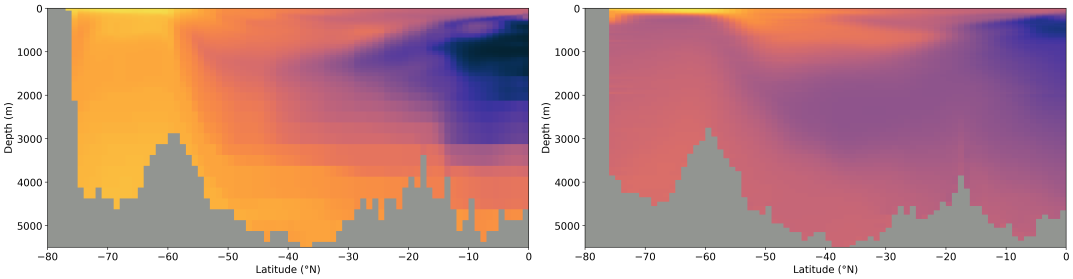

(c) NorESM2-MM, Pacific Ocean

(d) WOA18, Pacific Ocean

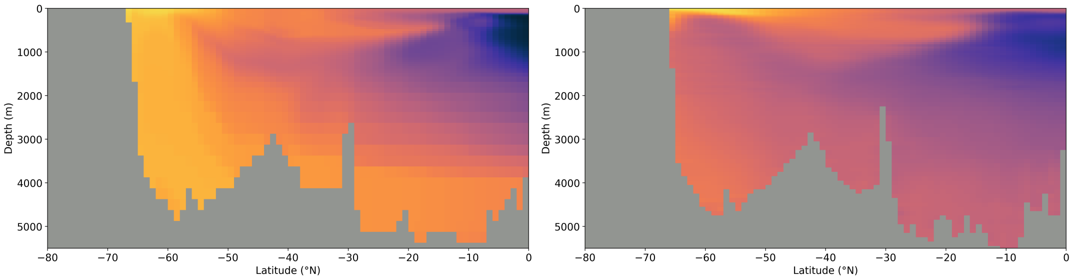

(e) NorESM2-MM, Indian Ocean

(f) WOA18, Indian Ocean

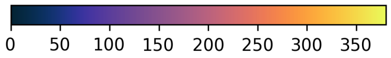

Figure 4.6: Mean concentrations of DO (µmol/L) in latitude-depth transects across three oceans. (a,b) represent the Atlantic Ocean, (c,d) the Pacific Ocean, and (e,f) the Indian Ocean. Data from NorESM2-MM historical simulations (1900–2014) in (a,c,e) and WOA18 observations (1900–2017) in (b,d,f).

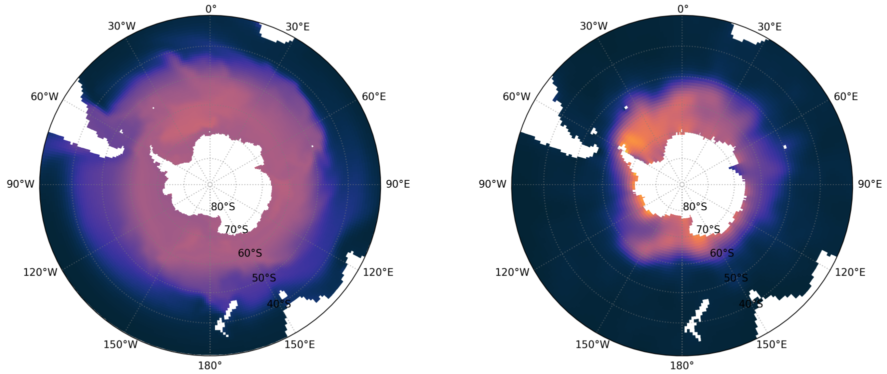

(a) NorESM2-MM, surface

(b) WOA18, surface

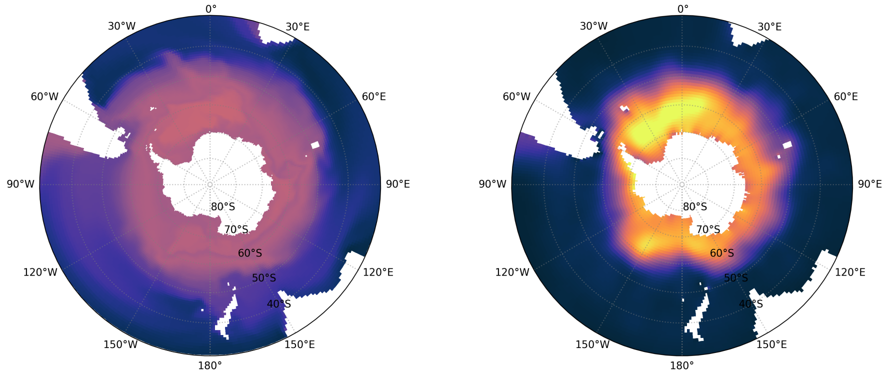

(c) NorESM2-MM, 250m depth

(d) WOA18, 250m depth

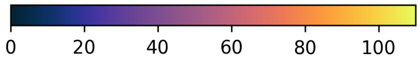

Figure 4.7: Mean concentrations of Si ($\mu mol/L$) in the Southern Ocean. (a,b) show surface data and (c,d) at 250m depth. Data from NorESM2-MM historical simulations (1900–2014) in (a,c) and WOA18 observations (1900–2017) in (b,d). Visualizations are projected using a South Polar Stereographic projection encompassing latitudes from $30°S$ to $90°S$.

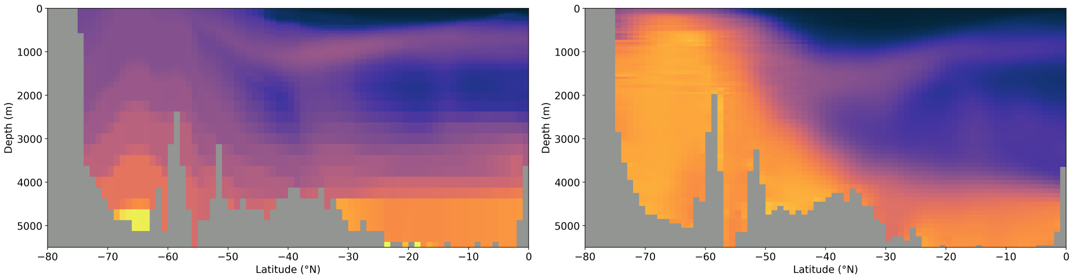

(a) NorESM2-MM, Atlantic Ocean

(b) WOA18, Atlantic Ocean

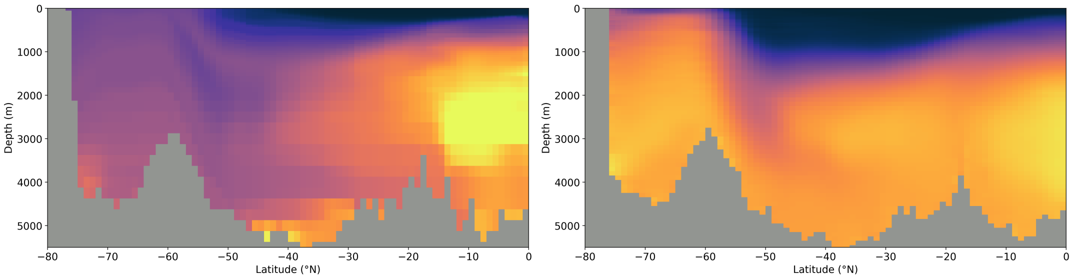

(c) NorESM2-MM, Pacific Ocean

(d) WOA18, Pacific Ocean

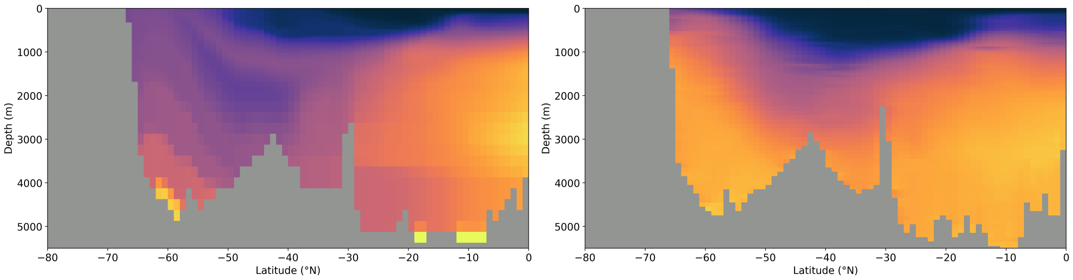

(e) NorESM2-MM, Indian Ocean

(f) WOA18, Indian Ocean

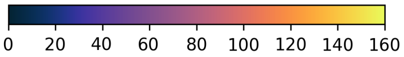

Figure 4.8: Mean concentrations of Si (µmol/L) in latitude-depth transects across three oceans. (a,b) represent the Atlantic Ocean, (c,d) the Pacific Ocean, and (e,f) the Indian Ocean. Data from NorESM2-MM historical simulations (1900–2014) in (a,c,e) and WOA18 observations (1900–2017) in (b,d,f).

4.2 Time Series Analysis

To help detect temporal variability, we examine the tracers' distribution along with the anomaly plots. All depths (surface, 100m, and 250m) exhibit a clear latitudinal gradient in tracer concentrations.

PO_4 shows high values around 49–55°S in the Atlantic (Figures 4.9a–c), around 54–59°S in the Pacific (Figures 4.9d–f), and 52–58°S in the Indian (Figures 4.9g–i). The concentration decreases moving northward from this latitude band. Similarly, moving southward from this band, the concentrations also show a slight decrease, indicating a different water mass influence. Surface PO_4 levels are subject to substantial changes due to turbulent mixing and interactions with the atmosphere, which are more pronounced in the upper layers of the ocean. At 100m depth, the impact of surface variability diminishes, leading to more stable concentration patterns compared to the surface. At 250m depth, the concentration patterns become even more stable compared with those two shallower depths, showing more persistent bands in the anomalies. The plots show temporal variability in PO_4 anomalies across all depths and oceans, with notable shifts occurring around the mid-20th century. In the pre-1930 period, positive anomalies predominate, especially south of 50°S, suggesting generally higher PO_4 concentrations during this period. After 1930, there was a notable shift to negative anomalies south of 50°S, indicating a reduction in PO_4 concentrations. The gradients, with higher PO_4 values around specific latitudes, suggest the presence of the SOBD. The identified latitude bands—around 49–55°S in the Atlantic, around 54–59°S in the Pacific, and around 52–58°S in the Indian—are consistent with previous studies that have identified these regions as zones of BGC transition (*Marinov et al.*, 2006; *Sarmiento et al.*, 2004).

At the surface and 100m depth, DO concentrations show a relatively stable pattern from 1850 to 2014, mostly close to zero in anomaly plots. At 250m depth, the latitudinal gradient is maintained, with lower overall oxygen concentrations compared to shallower depths. At this depth, temporal fluctuations are present in all sectors, with more pronounced variations in the Pacific sector compared to the Indian and Atlantic sectors. Also, our suggestion for the presence of the SOBD in this analysis is the transition from higher concentrations to lower concentrations around 49–55°S in the Atlantic (Figures 4.10a–c), around 54–59°S in the Pacific (Figures 4.10d–f), and around 52–58°S in the Indian (Figures 4.10g–i).

Overall, the concentrations of Si decrease moving northward and change rapidly around 50°S in the Atlantic, around 54°S in the Pacific, and around 52°S in the Indian. There is a pronounced period of reduction in Si concentrations from around 1930 to 1980, especially at higher latitudes, around 55–60°S in the Atlantic, around 60–70°S in the Pacific, and around 59–68°S in the Indian. As with the other two tracers, the SOBD location identified in this analysis is the transition from higher to lower concentrations: around 49–55°S in the Atlantic (Figures 4.11a–c), around 54–59°S in the Pacific (Figures 4.11d–f), and around 52–58°S in the Indian (Figures 4.11g–i).

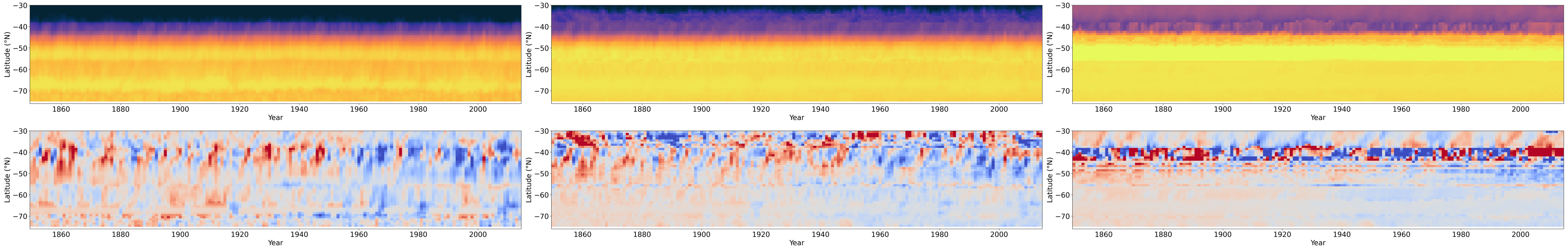

(a) Atlantic Sector, surface

(b) Atlantic Sector, 100m depth

(c) Atlantic Sector, 250m depth

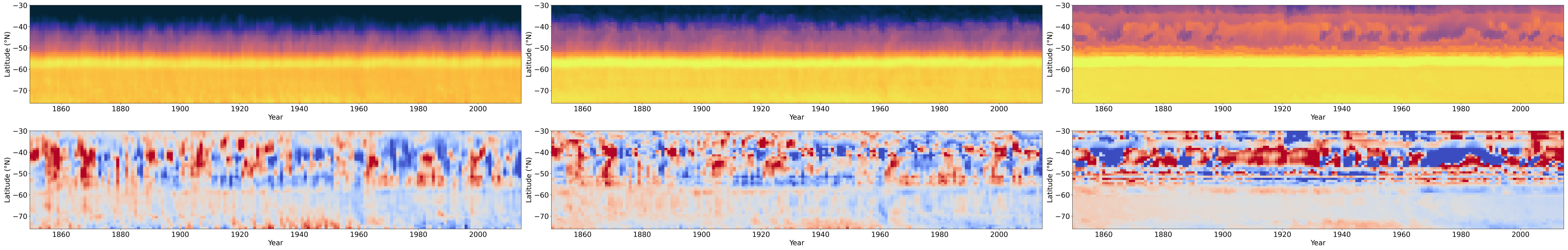

(d) Pacific Sector, surface

(e) Pacific Sector, 100m depth

(f) Pacific Sector, 250m depth

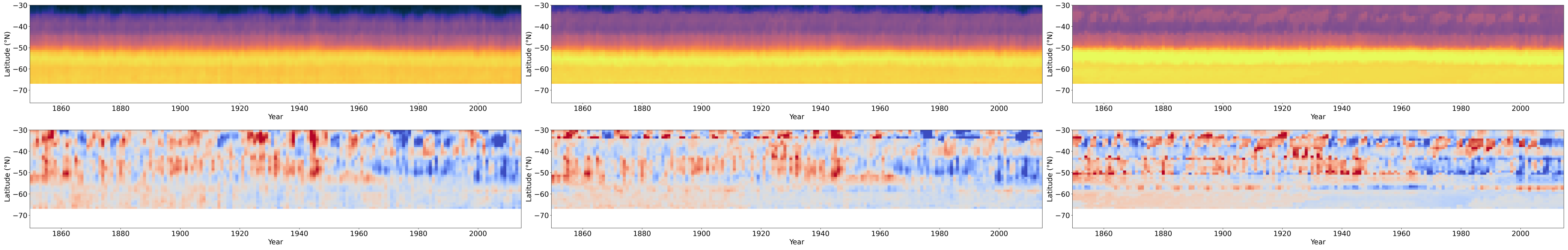

(g) Indian Sector, surface

(h) Indian Sector, 100m depth

(i) Indian Sector, 250m depth

Figure 4.9: Time series of mean PO_4 and anomaly (µmol/L) in (a–c) the Atlantic Sector, (d–f) the Pacific Sector, and (g–i) the Indian Sector of the Southern Ocean (from 1850 to 2014) across different depths: (a,d,g) surface; (b,e,h) 100m; (c,f,i) 250m. The x-axis represents years, and the y-axis represents latitude.

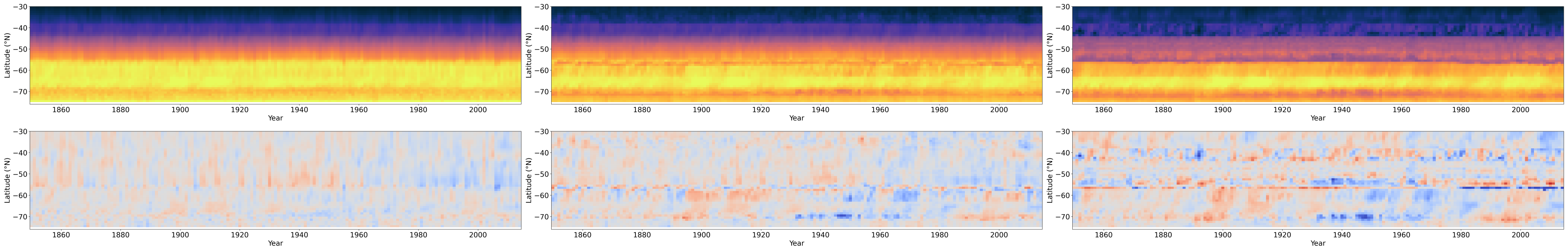

(a) Atlantic Sector, surface

(b) Atlantic Sector, 100m depth

(c) Atlantic Sector, 250m depth

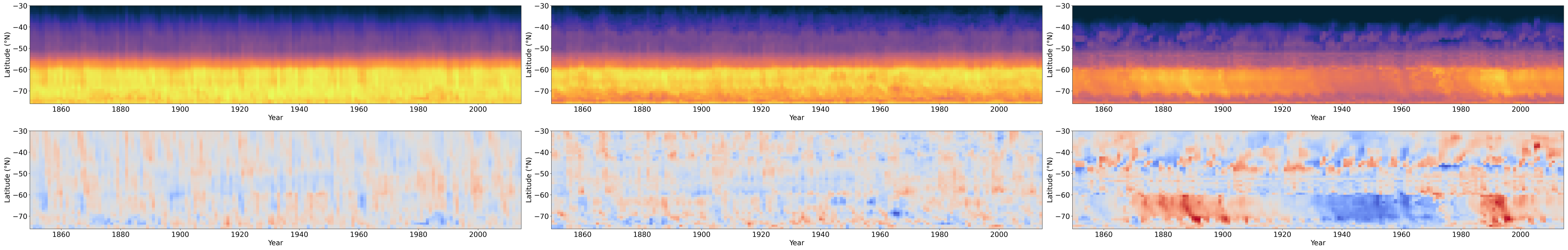

(d) Pacific Sector, surface

(e) Pacific Sector, 100m depth

(f) Pacific Sector, 250m depth

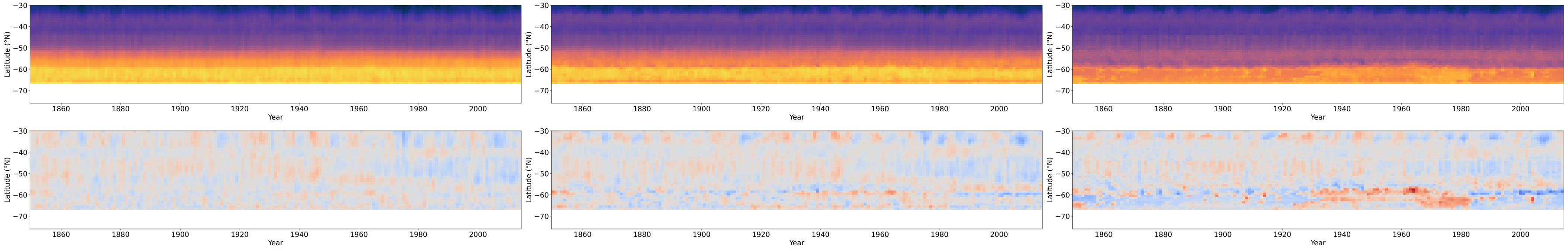

(g) Indian Sector, surface

(h) Indian Sector, 100m depth

(i) Indian Sector, 250m depth

Figure 4.10: Time series of mean DO and anomaly (µmol/L) in (a–c) the Atlantic Sector, (d–f) the Pacific Sector, and (g–i) the Indian Sector of the Southern Ocean (from 1850 to 2014) across different depths: (a,d,g) surface; (b,e,h) 100m; (c,f,i) 250m. The x-axis represents years, and the y-axis represents latitude.

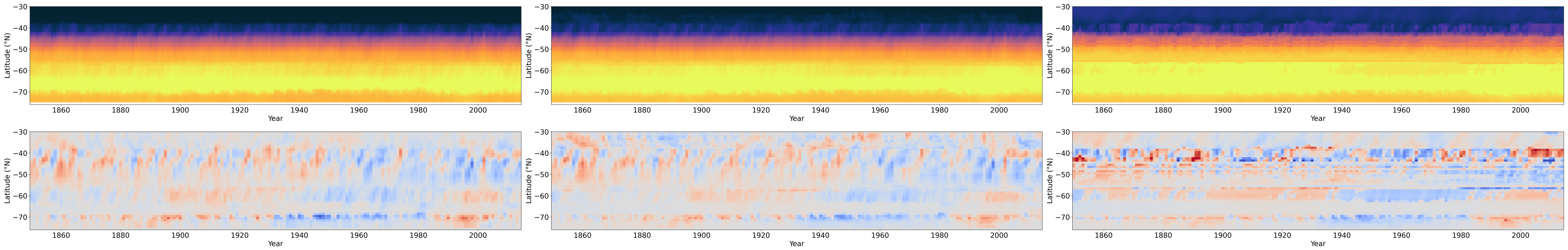

(a) Atlantic Sector, surface

(b) Atlantic Sector, 100m depth

(c) Atlantic Sector, 250m depth

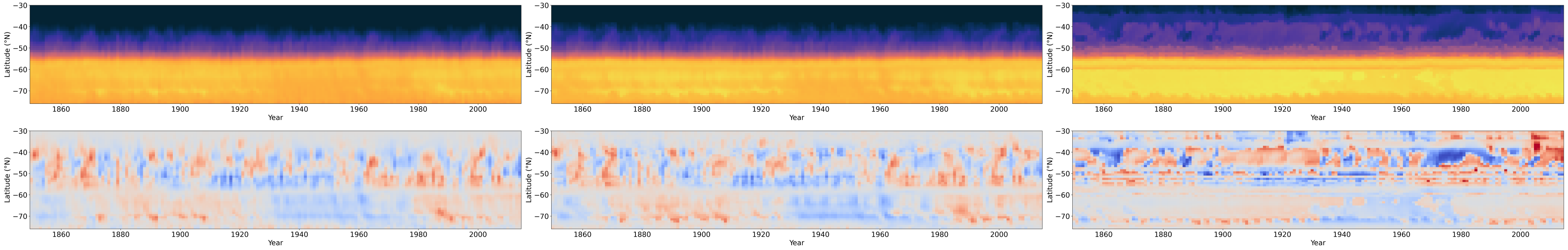

(d) Pacific Sector, surface

(e) Pacific Sector, 100m depth

(f) Pacific Sector, 250m depth

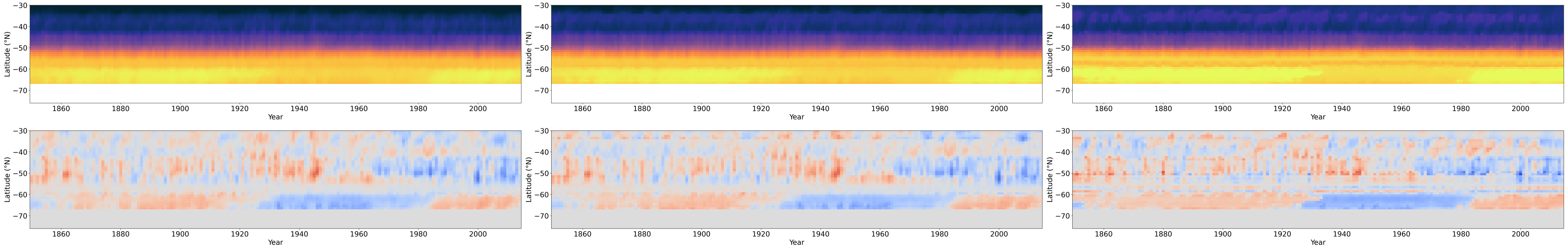

(g) Indian Sector, surface

(h) Indian Sector, 100m depth

(i) Indian Sector, 250m depth

Figure 4.11: Time series of mean Si and anomaly (µmol/L) in (a–c) the Atlantic Sector, (d–f) the Pacific Sector, and (g–i) the Indian Sector of the Southern Ocean (from 1850 to 2014) across different depths: (a,d,g) surface; (b,e,h) 100m; (c,f,i) 250m. The x-axis represents years, and the y-axis represents latitude.

The piControl (Pre-industrial Control) experiment is one of the standard experiments in climate modeling, particularly within the CMIP framework. The piControl experiment serves as a baseline for understanding natural variability and the system's response to anthropogenic and other external forcings. It represents the climate system in a stable state and includes natural forcings such as solar radiation and volcanic activity, but no changes in greenhouse gas concentrations, aerosols, or land use due to human activities. These forcings are held constant at pre-industrial levels. The experiment is run for a long period, 150 years (1550–1699), to ensure that the climate system reaches and maintains equilibrium. This long duration helps to average out internal climate variability and provides a stable reference state.

Figure 4.12 shows historical simulations and piControl of Si anomalies in the Atlantic sector of the Southern Ocean across three different depths. The results of the piControl experiment exhibit natural climate variability without any long-term trends or shifts and oscillate around zero, indicating no persistent deviation from the long-term mean. The historical simulations across three depths show more variability than the piControl. We observe some temporal and spatial patterns of natural variability, for example, at 250m depth—showing some pronounced variability around 40°S (above our suggested SOBD location)—but these patterns are not as strong as those in the historical simulations.

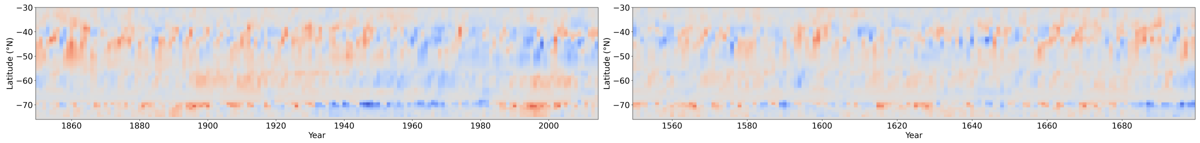

(a) historical Si, surface

(b) piControl Si, surface

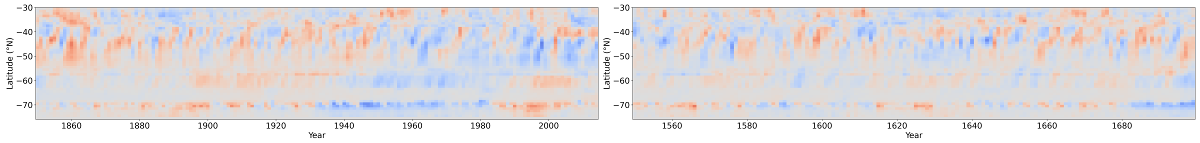

(c) historical Si, 100m depth

(d) piControl Si, 100m depth

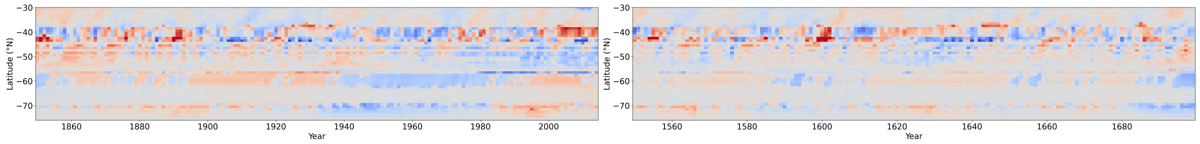

(e) historical Si, 250m depth

(f) piControl Si, 250m depth

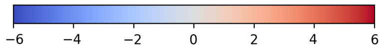

Figure 4.12: (a,c,e) Historical simulations (1850–2014) and (b,d,f) piControl (1550–1699) of Si (μmol/L) anomalies in the Atlantic Sector of the Southern Ocean across different depths: (a,b) surface; (c,d) 100m; (e,f) 250m. The x-axis represents years, and the y-axis represents latitude. Data from NorESM2-MM.

The time series analysis results show no significant change in the location of the SOBD over the study period (1850 to 2014). This stability is observed across all three ocean sectors (Atlantic, Pacific, and Indian) and at various depths (surface, 100m, and 250m). While the overall location of the SOBD remains stable, there are notable regional differences in the variability of BGC tracers. The Atlantic sector shows relatively stable BGC patterns with minor temporal fluctuations, indicating a less dynamic environment compared to the other sectors. The Pacific sector exhibits more pronounced variability in both DO and Si concentrations, suggesting stronger influences from regional oceanographic and climatic processes. The Indian sector also shows significant temporal fluctuations, particularly in Si concentrations, highlighting the dynamic nature of this sector.

Anomalies plots of all tracers show a shift from positive to negative values south of the SOBD around 1930 (this pattern does not apply to DO in the Indian sector, where DO shows a shift in the same period but in the opposite direction). We associate this shift with the Early Twentieth Century Warming (ETCW)—the most pronounced warming in the historical global climate record prior to recent warming, which occurred over the first half of the 20th century (*Hegerl et al.*, 2018). The ETCW featured a significant Arctic warming in the 1920s and 1930s and included several important climatic anomalies, such as Indian monsoon failures in the 1900s (*Wang*, 2006; *Zhou et al.*, 2010), the North American Dust Bowl droughts and record-breaking heat waves in the 1930s (*Cook et al.*, 2009; *Cowan et al.*, 2017; *Donat et al.*, 2016; *Schubert et al.*, 2004), the cold European winters of 1940–1942 (*Brönnimann et al.*, 2004), and the World War II period drought in Australia between 1937 and 1945 (*Verdon-Kidd and Kiem*, 2009). The European summer droughts and heat waves of the mid and late 1940s (*Sutton and Hodson*, 2005), such as the 1947 heatwave (*Schär et al.*, 2004), followed these anomalously cold winters during WWII. Research supports that the early 20th century shows a pronounced period of warming, with increases in land, ocean, and global temperature anomalies (*Anderson et al.*, 2013; *Crowley et al.*, 2014; *Hegerl et al.*, 2018; *Kennedy et al.*, 2011; *Morice et al.*, 2012). *Callendar* (1938) already attributed the ETCW to increased CO_2 concentrations in the late 1930s. Global climate anomalies also occurred during the 19391942 El Niño (*Brönnimann et al.*, 2004). However, very little information is available about the Southern Ocean during that period (*Hegerl et al.*, 2018). We also relate this shift to the Southern Annular Mode (SAM) index. The SAM index, which quantifies the pressure difference between the mid-latitudes and the high latitudes of the Southern Hemisphere, impacts the strength of the westerly winds. Around 1930 (Figure 4.13), the SAM index shows a significant deviation from about 1.7 to -2.5 (approximately a 4.2 difference), which could be related to the ETCW.

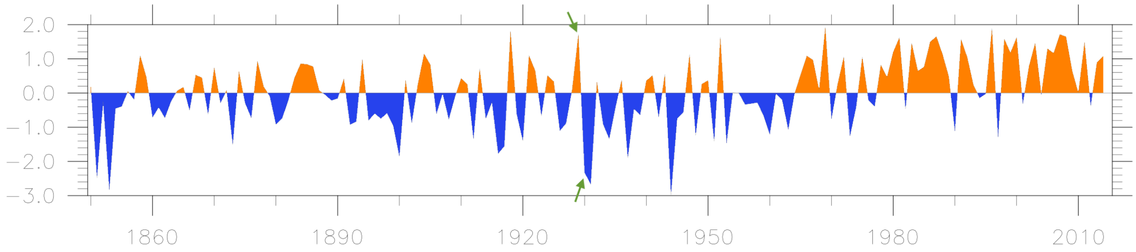

Figure 4.13: The SAM index (annual) from 1850 to 2014. Green arrows indicate the period around 1930, where there is a significant deviation in the index (more than a 4-point difference). Data sourced NorESM2-MM, plotted using the ESMValTool (Bentsen et al., 2019; Phillips et al., 2014; Righi et al., 2020).

The SAM index shifted to positive values after 1965, corresponding to stronger westerly winds directed southward. These stronger winds enhance upwelling (*Anderson et al.*, 2009). This process can be related to DO and Si shifting back to positive valuesobserved increases in DO and Si concentrations post-1980 (this pattern does not apply to DO in the Indian sector, where DO shows a shift in the same period but in the opposite direction). The shift around 1980 is likely linked to the study by *Keppler and Landschützer* (2019), which shows that during the analysis period (1982–2016), the average SAM index showed positive values correlated with more ocean CO_2 uptake.

4.2.1 Seasonal Effect

The results show the seasonal variations of the BGC tracers concentrations in the Southern Ocean across different depths and sectors in Figures 4.14–4.16. The tracers concentrations at the surface show seasonal variability. At 100m depth, their concentrations exhibit a more uniform distribution with less pronounced seasonal variation compared to the surface. At 250m depth, the concentrations are more stable throughout the year compared with the sallower depths. This pattern is consistent across all sectors.

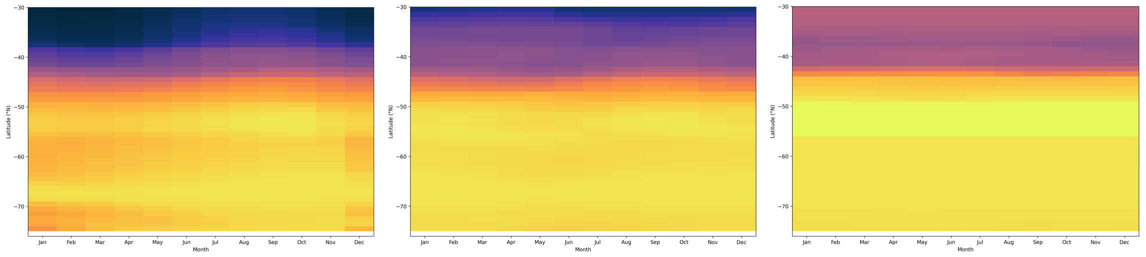

(a) Atlantic, surface *(b) Atlantic, 100m depth* *(c) Atlantic, 250m depth*

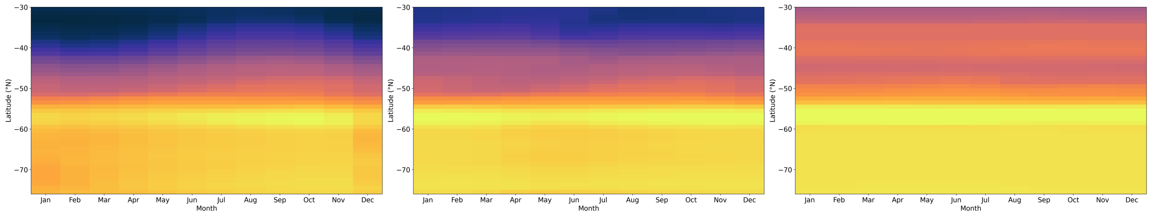

(d) Pacific, surface *(e) Pacific, 100m depth* *(f) Pacific, 250m depth*

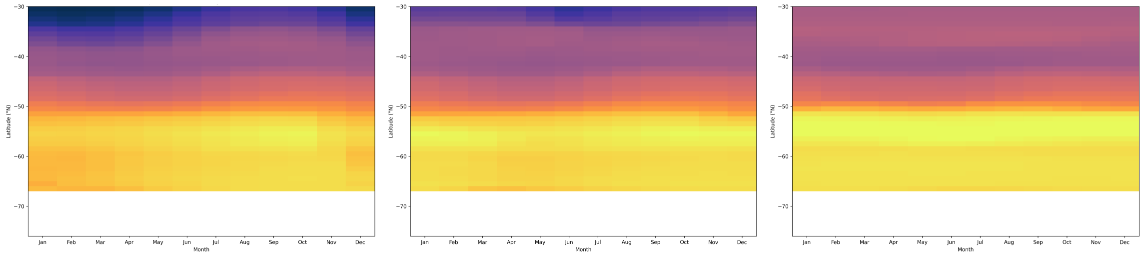

(g) Indian, surface *(h) Indian, 100m depth* *(i) Indian, 250m depth*

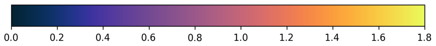

Figure 4.14: Monthly mean PO_4 concentrations ($\mu mol/L$) in (a–c) the Atlantic Sector, (d–f) the Pacific Sector, and (g–i) the Indian Sector of the Southern Ocean (from 1850 to 2014) across different depths: (a,d,g) Surface; (b,e,h) 100m; (c,f,i) 250m. The x-axis represents months, and the y-axis represents latitude.

The SOBD locations shown in each sector are still the same as in the previous analysis. This stability at 250m depth makes it a suitable layer to examine the SOBD location. The lack of seasonal variability at this depth allows for a clearer identification and analysis of the SOBD, minimizing the influence of short-term surface processes.

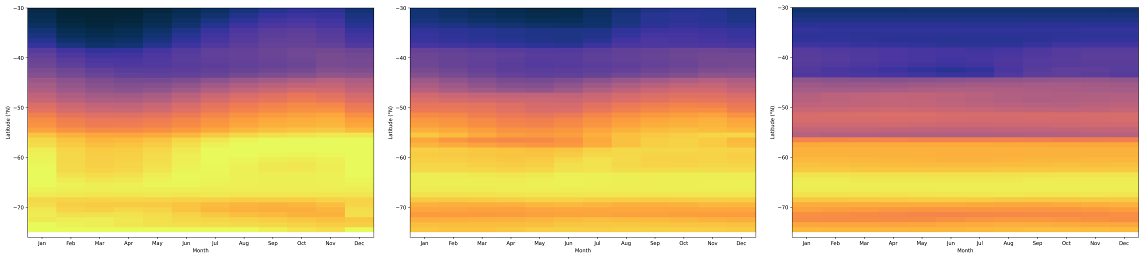

(a) Atlantic, surface *(b) Atlantic, 100m depth* *(c) Atlantic, 250m depth*

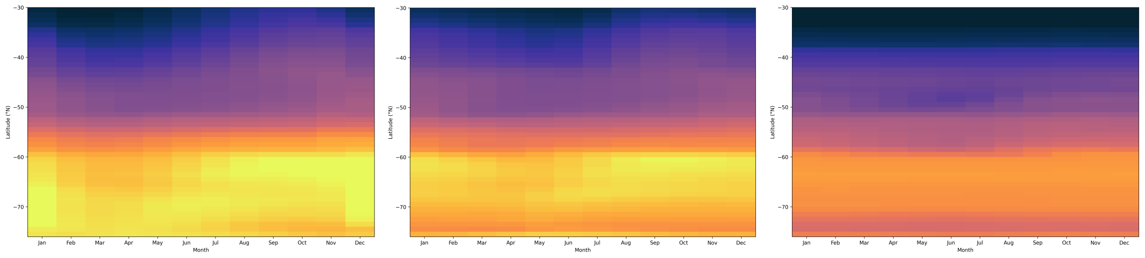

(d) Pacific, surface *(e) Pacific, 100m depth* *(f) Pacific, 250m depth*

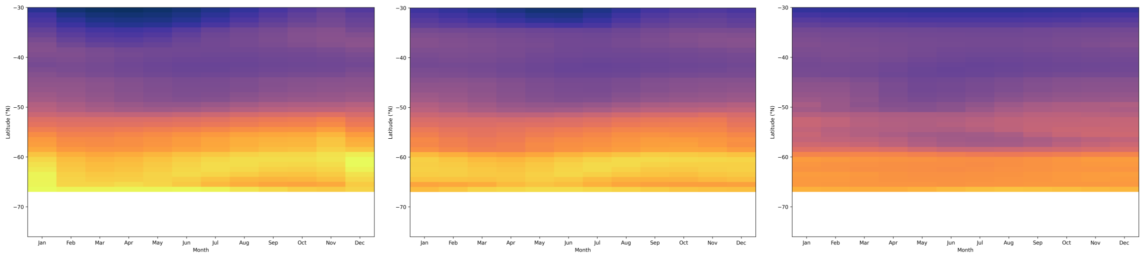

(g) Indian, surface *(h) Indian, 100m depth* *(i) Indian, 250m depth*

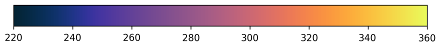

Figure 4.15: Monthly mean DO concentrations (µmol/L) in (a–c) the Atlantic Sector, (d–f) the Pacific Sector, and (g–i) the Indian Sector of the Southern Ocean (from 1850 to 2014) across different depths: (a,d,g) Surface; (b,e,h) 100m; (c,f,i) 250m. The x-axis represents months, and the y-axis represents latitude.

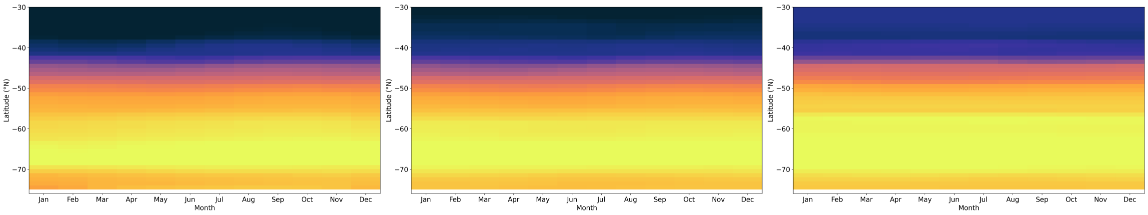

(a) Atlantic, surface *(b) Atlantic, 100m depth* *(c) Atlantic, 250m depth*

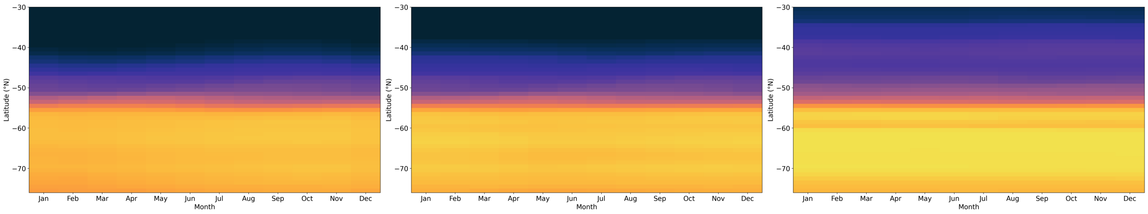

(d) Pacific, surface *(e) Pacific, 100m depth* *(f) Pacific, 250m depth*

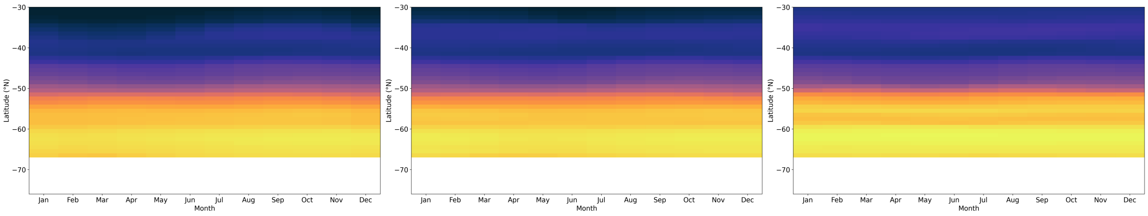

(g) Indian, surface *(h) Indian, 100m depth* *(i) Indian, 250m depth*

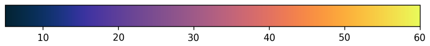

Figure 4.16: Monthly mean Si concentrations (μmol/L) in (a–c) the Atlantic Sector, (d–f) the Pacific Sector, and (g–i) the Indian Sector of the Southern Ocean (from 1850 to 2014) across different depths: (a,d,g) Surface; (b,e,h) 100m; (c,f,i) 250m. The x-axis represents months, and the y-axis represents latitude.

One significant advantage of the NorESM2-MM model is its ability to provide long-term historical simulations. This capability can be used to investigate the temporal variability of BGC tracers such as PO_4, DO, and Si over different timescales. Researchers can analyze seasonal, interannual, and decadal variations to understand how these nutrients and oxygen levels fluctuate in response to natural climate variability and anthropogenic influences. This temporal analysis can help identify trends and patterns that are not apparent from short-term observational data alone.

4.3 The Southern Ocean Biogeochemical Divide Location

To give us a broad overview of the SOBD, we plotted the BGC tracers with the 1036.5 kg/m^3 isopycnal line at 250m, as this depth is our suitable layer to examine the SOBD location. In Figure 4.17, PO_4, DO, and Si concentrations range from approximately 1.0–1.8, 220–340, and 20–60 μmol/L, respectively. Both nutrients show higher levels observed near the Antarctic continent, particularly around coastal regions, and lower concentrations further north. The isopycnal line at 1036.5 kg/m^3 indicates the boundary between different water masses, coinciding with significant changes in nutrient concentrations. This distribution highlights the influence of upwelling CDW in bringing nutrient-rich waters to the surface in the Southern Ocean, which refers to the SOBD location. DO levels show higher concentrations closer to the Antarctic continent. The isopycnal line at 1036.5 kg/m^3 marks a boundary where DO levels change, reflecting the influence of physical and biological processes. Higher oxygen concentrations are associated with regions of intense mixing and upwelling, while lower levels further north indicate less mixing and potential oxygen consumption by biological activity. The transition from higher concentrations to lower concentrations represents the SOBD. In Figure 4.17b,e,h, the plots suggest that the SOBD location falls between the PF and the SB of the ACC. Additionally, Figure 4.17c,f,i show that in some regions, the SOBD overlaps with the SACCF.

The results of this study align with *Xie et al.* (2022). They localized the SOBD by releasing virtual Lagrangian particles south of 40°S in an eddying ocean sea-ice model and compared simulation results with observations. They identified the SOBD as a circumpolar band shaped by different oceanographic features in various sectors, such as Ekman transport, the γ = 27.6 kg/m^3 neutral density outcrop as the dividing line between the upper and lower cells, and fronts associated with the ACC. Our SOBD location falls between the SAF (*Sokolov and Rintoul*, 2009) and the SB (*Orsi et al.*, 1995) associated with the ACC. However, our suggested location of the SOBD is narrower, as we consider the surface to 250m depth, whereas they consider deeper depths down to 500m.

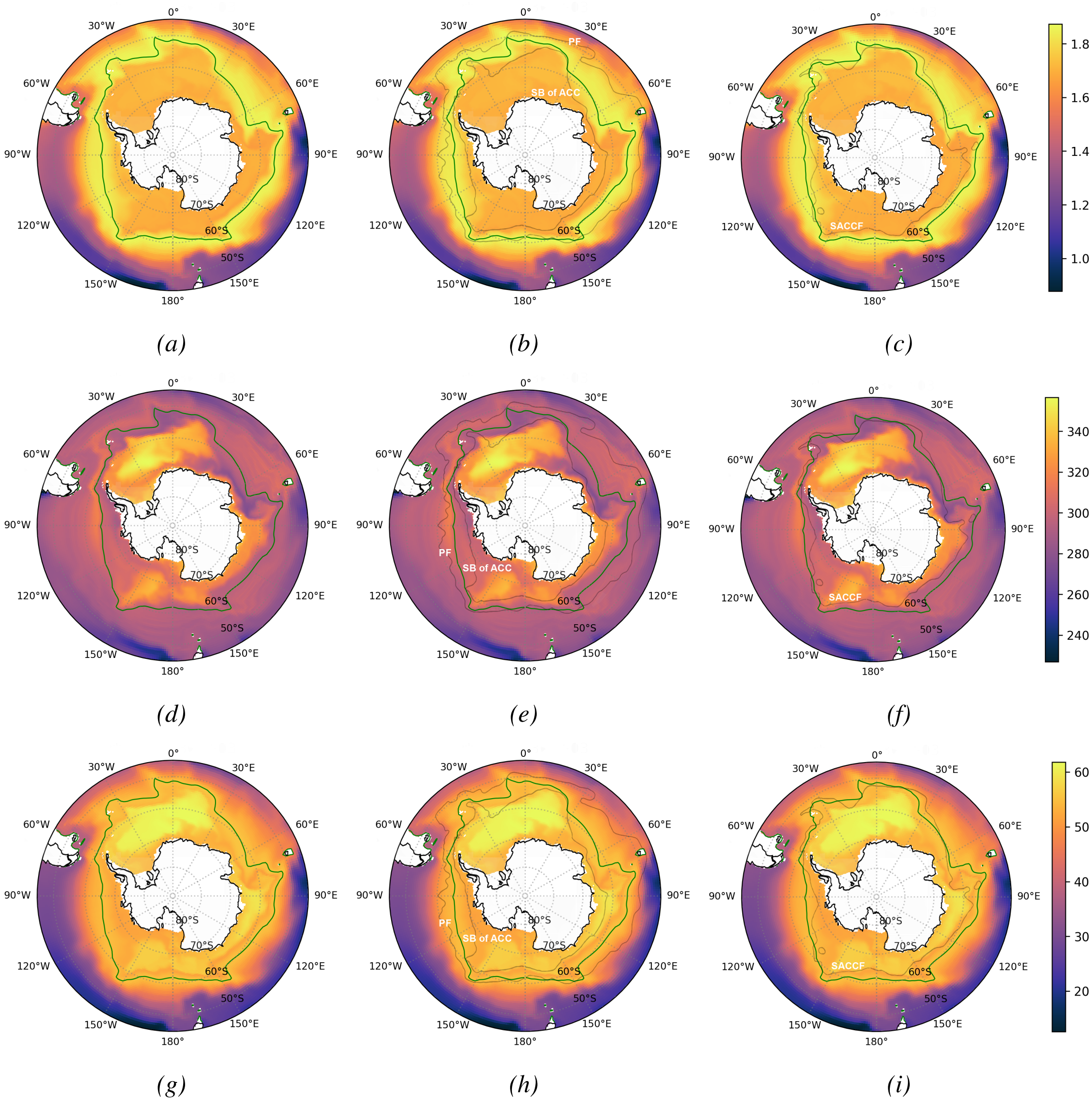

(a) (b) (c)

(d) (e) (f)

(g) (h) (i)

Figure 4.17: Mean concentrations of (a–c) PO_4, (d–f) DO, and (g–i) Si ($\mu mol/L$) at 250m depth in the Southern Ocean from 1850–2014. A green line shows the isopycnal line at 1036.5 kg/m^3. In (b,e,h,), the grey lines show the position of PF and SB of ACC. In (c,f,i), the grey line shows the position of SACCF. Visualizations are projected using a South Polar Stereographic projection encompassing latitudes from 45°S to 90°S.

The results have demonstrated that NorESM2-MM is capable of reproducing an upwelling region surrounding the Antarctic continent, and that the location of this region remains fairly stable over time. Hence it is unlikely that variability of the location of the SOBD has played a major role in shifting the net nutrient transport either northward or southward during the historical period. However, the BGC tracer fields transported by the overturning water masses seem to change over time. Although the location of the SOBD does not seem to change much, we have not investigated if there are fluctuations in the volume transport itself. For the wind fields, we only examined the SAM index and did not perform a detailed analysis. However, there are indications of long-term oscillations in volume transport through the Drake Passage, suggesting that the transport system is not constant over the historical period (see Figure 7 from *Seland et al.* (2020)).

Chapter 5

Conclusions

5.1 Key Findings

5.1.1 Biogeochemical Tracers Distribution

Distribution patterns of BGC tracers showed that PO_4 concentrations in the model were around 1.5 μmol/L at the surface, peaking at 1.9 μmol/L at 250m depth. A gradual decrease in PO_4 concentrations was observed moving northward from 50°S. The distribution of DO showed higher concentrations, approximately 360 μmol/L, near the Antarctic continent at the surface, decreasing with depth. For Si, surface concentrations were around 45 μmol/L, with higher values around 60 μmol/L at 250m depth. The distribution pattern of Si was similar to that of PO_4 but with generally higher concentrations. When compared with observational data, the NorESM2-MM model generally underestimated nutrient concentrations but overestimated DO compared to WOA18 observations. While the NorESM2-MM model underestimated PO_4 concentrations compared to observational data, it successfully captured the overall spatial patterns and vertical gradients of PO_4 distribution. Si concentrations were nearly twice as high in the WOA18 data compared to the model. Both datasets show a gradual decrease in Si concentrations moving northwards, but WOA18 starts showing this trend around 60°S, while the NorESM2-MM data starts around 50°S. While surface DO distributions were similar, significant differences were noted at deeper depths, where WOA18 showed a ring of low DO surrounding Antarctica not captured by the model.

Latitude-depth transects show that BGC tracers effectively capture ocean circulation patterns and distinguish between different water masses. It appears that the model represents the concentration of tracers in AABW (in the Southern Ocean and near the bottom) differently from the observational data. The model underestimates the nutrients (PO_4 and Si) and overestimates DO in this water mass.

5.1.2 Time Series Analysis

The distributions of PO_4, DO, and Si exhibit clear latitudinal gradients and consistent patterns across various depths (surface, 100m, and 250m). The BGC tracer distributions show transitions in specific latitude bands, suggesting the presence of the SOBD. Time series analysis revealed significant temporal fluctuations in the concentrations of BGC tracers, with notable shifts occurring around the mid-20th century. Before

1930, positive anomalies predominated, indicating higher nutrient concentrations. After 1930, a shift to negative anomalies was observed, suggesting a reduction in nutrient levels. The ETCW was identified as a potential driver for the observed shifts, with significant climate anomalies such as the pronounced warming in the 1920s and 1930s and associated changes in global climatic conditions. The SAM index also showed a significant deviation around 1930, correlating with the ETCW and influencing the strength of westerly winds and upwelling processes in the Southern Ocean.

The SOBD location found in this analysis is around 49–55°S in the Atlantic sector, around 54–59°S in the Pacific sector, and around 52–58°S in the Indian sector. The SOBD remained stable over the study period (1850 to 2014).

Seasonal variations in tracer concentrations were observed at the surface, with more uniform distribution and less pronounced seasonal variation at 100m and 250m depths. This pattern was consistent across all sectors. The stability at 250m depth, compared to shallower depths, makes it a suitable layer for examining long-term trends and minimizing the influence of short-term surface processes.

5.1.3 The Southern Ocean Biogeochemical Divide Location

The analysis indicates that the SOBD can be reliably identified at approximately 250m depth, where significant changes in nutrient concentrations align with the 1036.5 $\mathrm{kg/m^3}$ isopycnal line. This depth captures the transition between nutrient-rich waters upwelled near Antarctica and nutrient-depleted waters further north, providing a clear marker for the SOBD. The isopycnal line at 1036.5 $\mathrm{kg/m^3}$ effectively marks the boundary between different water masses, coinciding with significant changes in nutrient concentrations and DO levels. This line helps identify the SOBD's location, which falls between the PF and the SB of the ACC.

The results align with the findings of *Xie et al.* (2022), who localized the SOBD using virtual Lagrangian particles in an eddying ocean sea-ice model. Both studies identified the SOBD as a circumpolar band shaped by various oceanographic features and fronts associated with the ACC. However, our study suggested a narrower SOBD location, considering the surface to 250m depth, compared to the deeper depths (down to 500m) considered by *Xie et al.* (2022).

5.2 Contributions

This study provides a detailed comparison of BGC tracers in the Southern Ocean, enhancing our understanding of nutrient dynamics and the SOBD. The use of both model simulations and observational data allows for a comprehensive analysis, highlighting the strengths and weaknesses of the NorESM2. The identification of the SOBD over time provides valuable insights into the Southern Ocean's role in global BGC cycles.

5.3 Model Evaluation and Improvement

One significant advantage of the NorESM2 is its ability to provide long-term historical simulations. The NorESM2 demonstrates a reasonable ability to replicate broad patterns of BGC tracer distributions. However, it tends to underestimate nutrient concentrations and overestimate dissolved oxygen levels, especially in the Southern Ocean. Discrepancies between the model and observational data highlight areas for improvement, such as the representation of nutrient cycling, organic matter decomposition, and vertical mixing processes.

5.4 Future Work

Future work should focus on incorporating more advanced statistical analyses, such as correlation and regression techniques, to enhance the understanding of the BGC processes in the Southern Ocean. Specifically for our findings, research should delve deeper into the relationship between Si concentrations and the SAM index, as initial findings suggest a strong alignment between these variables, necessitating a more detailed analysis to identify trends and correlations. This could involve calculating correlation coefficients to quantify the relationship's strength and direction, and examining the slope of the regression fit between Si anomalies and the SAM index would provide insights into how changes in the SAM index influence Si concentrations. Such analyses will enhance our understanding of the interplay between atmospheric and oceanic processes in the Southern Ocean.

While the current study provides a broad overview of BGC tracer distributions, the NorESM2 can be used for more detailed regional analyses. Focusing on specific areas such as the Weddell Sea, Ross Sea, or the ACC can reveal finer-scale processes and interactions that are not captured in a broader analysis. Detailed regional studies can also help validate the model against localized observational data, improving its accuracy and reliability.

The comprehensive representation of marine and atmospheric systems in NorESM2 allows for coupled atmosphere-ocean analysis. Future research should leverage this capability to study the interactions between atmospheric conditions, such as wind patterns and temperature, and oceanic processes, such as upwelling and nutrient cycling. Understanding these combined impacts on BGC tracers will enhance our knowledge of the Southern Ocean's dynamics.

Refining the model's representation of BGC processes and incorporating more detailed observational data is crucial for improving the accuracy and reliability of climate projections. By continuously comparing model outputs with new and existing observational datasets, researchers can identify discrepancies and areas where the model needs improvement. Expanding the tracer analysis to include additional BGC tracers such as nitrate, iron, and carbon will provide a more comprehensive understanding of nutrient dynamics and BGC processes.

Integrating high-resolution observational data from satellite remote sensing, autonomous floats, and research cruises will be vital for validating and refining model outputs. These efforts will improve the accuracy of climate models and enhance our ability to predict future changes. Investigating the potential impacts of climate change on the SOBD and nutrient cycling in the Southern Ocean is another critical area for future research. Understanding how changing atmospheric and oceanic conditions affect these processes will be essential for predicting and mitigating the effects of climate change.

Finally, adopting interdisciplinary approaches that combine physical, chemical, and biological oceanography will be crucial for developing a holistic understanding of the Southern Ocean's BGC processes and their global implications. Such approaches will provide a more integrated perspective, leading to better-informed strategies for marine conservation and climate change mitigation.

Bibliography

Anderson, D. M., E. M. Mauk, E. R. Wahl, C. Morrill, A. J. Wagner, D. Easterling, and T. Rutishauser (2013), Global warming in an independent record of the past 130 years, *Geophysical Research Letters*, *40*(1), 189–193, doi:https://doi.org/10.1029/2012GL054271. 4.2

Anderson, R. F., Z. Chase, M. Q. Fleisher, and J. Sachs (2002), The southern ocean's biological pump during the last glacial maximum, *Deep Sea Research Part II: Topical Studies in Oceanography*, *49*(9), 1909–1938, doi:https://doi.org/10.1016/S0967-0645(02)00018-8, the Southern Ocean I: Climatic Changes in the Cycle of Carbon in the Southern Ocean. 2.2.3

Anderson, R. F., S. Ali, L. I. Bradtmiller, S. H. H. Nielsen, M. Q. Fleisher, B. E. Anderson, and L. H. Burckle (2009), Wind-driven upwelling in the southern ocean and the deglacial rise in atmospheric co2, *Science*, *323*(5920), 1443–1448, doi:10.1126/science.1167441. 4.2

Baines, S. B., B. S. Twining, M. A. Brzezinski, D. M. Nelson, and N. S. Fisher (2010), Causes and biogeochemical implications of regional differences in silicification of marine diatoms, *Global Biogeochemical Cycles*, *24*(4), doi:https://doi.org/10.1029/2010GB003856. 2.2.2

Benitez-Nelson, C. R. (2000), The biogeochemical cycling of phosphorus in marine systems, *Earth-Science Reviews*, *51*(1), 109–135, doi:https://doi.org/10.1016/S0012-8252(00)00018-0. (document), 2.5

Bentsen, M., I. Bethke, J. B. Debernard, T. Iversen, A. Kirkevåg, Ø. Seland, H. Drange, C. Roelandt, I. A. Seierstad, C. Hoose, and J. E. Kristjánsson (2013), The norwegian earth system model, noresm1-m – part 1: Description and basic evaluation of the physical climate, *Geoscientific Model Development*, *6*(3), 687–720, doi:10.5194/gmd-6-687-2013. 3.1.1

Bentsen, M., D. J. L. Oliviè, y. Seland, T. Toniazzo, A. Gjermundsen, L. S. Graff, J. B. Debernard, A. K. Gupta, Y. He, A. Kirkevåg, J. Schwinger, J. Tjiputra, K. S. Aas, I. Bethke, Y. Fan, J. Griesfeller, A. Grini, C. Guo, M. Ilicak, I. H. H. Karset, O. A. Landgren, J. Liakka, K. O. Moseid, A. Nummelin, C. Spensberger, H. Tang, Z. Zhang, C. Heinze, T. Iversen, and M. Schulz (2019), Ncc noresm2-mm model output prepared for cmip6 cmip historical, doi:10.22033/ESGF/CMIP6.8040. (document), 4.13

Boyd, P. W. (2002), Environmental factors controlling phytoplankton processes in the southern ocean1, *Journal of Phycology*, *38*(5), 844–861, doi:https://doi.org/10.1046/j.1529-8817.2002.t01-1-01203.x. 2.2.2

Boyd, P. W., and M. J. Ellwood (2010), The biogeochemical cycle of iron in the ocean, *Nature Geoscience*, *3*(10), 675–682. 2.2.2

Brönnimann, S., J. Luterbacher, J. Staehelin, T. Svendby, G. Hansen, and T. Svenøe (2004), Extreme climate of the global troposphere and stratosphere in 1940–42 related to el niño, *Nature*, *431*(7011), 971–974. 4.2

Buesseler, K. O., and P. W. Boyd (2009), Shedding light on processes that control particle export and flux attenuation in the twilight zone of the open ocean, *Limnology and Oceanography*, *54*(4), 1210–1232, doi:https://doi.org/10.4319/lo.2009.54.4.1210. 1

Callendar, G. S. (1938), The artificial production of carbon dioxide and its influence on temperature, *Quarterly Journal of the Royal Meteorological Society*, *64*(275), 223–240, doi:https://doi.org/10.1002/qj.49706427503. 4.2

Cavan, E., A. Belcher, A. Atkinson, S. Hill, S. Kawaguchi, S. McCormack, B. Meyer, S. Nicol, L. Ratnarajah, K. Schmidt, et al. (2019), The importance of antarctic krill in biogeochemical cycles, *Nature communications*, *10*(1), 4742. 2.2.1

Chapman, C. C., M.-A. Lea, A. Meyer, J.-B. Sallée, and M. Hindell (2020), Defining southern ocean fronts and their influence on biological and physical processes in a changing climate, *Nature Climate Change*, *10*(3), 209–219. 2.2.1, 2.2.1

Cook, B. I., R. L. Miller, and R. Seager (2009), Amplification of the north american “dust bowl” drought through human-induced land degradation, *Proceedings of the National Academy of Sciences*, *106*(13), 4997–5001, doi:10.1073/pnas.0810200106. 4.2

Cowan, T., G. C. Hegerl, I. Colfescu, M. Bollasina, A. Purich, and G. Boschat (2017), Factors contributing to record-breaking heat waves over the great plains during the 1930s dust bowl, *Journal of Climate*, *30*(7), 2437 – 2461, doi:10.1175/JCLI-D-16-0436.1. 4.2

Crowley, T. J., S. P. Obrochta, and J. Liu (2014), Recent global temperature “plateau” in the context of a new proxy reconstruction, *Earth’s Future*, *2*(5), 281–294, doi:https://doi.org/10.1002/2013EF000216. 4.2

Danabasoglu, G., J.-F. Lamarque, J. Bacmeister, D. A. Bailey, A. K. DuVivier, J. Edwards, L. K. Emmons, J. Fasullo, R. Garcia, A. Gettelman, C. Hannay, M. M. Holland, W. G. Large, P. H. Lauritzen, D. M. Lawrence, J. T. M. Lenaerts, K. Lindsay, W. H. Lipscomb, M. J. Mills, R. Neale, K. W. Oleson, B. Otto-Bliesner, A. S. Phillips, W. Sacks, S. Tilmes, L. van Kampenhout, M. Vertenstein, A. Bertini, J. Dennis, C. Deser, C. Fischer, B. Fox-Kemper, J. E. Kay, D. Kinnison, P. J. Kushner, V. E. Larson, M. C. Long, S. Mickelson, J. K. Moore, E. Nienhouse, L. Polvani, P. J. Rasch, and W. G. Strand (2020), The community earth system model version 2 (cesm2), *Journal of Advances* *in Modeling Earth Systems*, *12*(2), e2019MS001,916, doi:https://doi.org/10.1029/2019MS001916, e2019MS001916 2019MS001916. 3.1.1

Davila, X., G. Gebbie, A. Brakstad, S. K. Lauvset, E. L. McDonagh, J. Schwinger, and A. Olsen (2022), How is the ocean anthropogenic carbon reservoir filled?, *Global Biogeochemical Cycles*, *36*(5), e2021GB007,055, doi:https://doi.org/10.1029/2021GB007055, e2021GB007055 2021GB007055. 2.1

de Baar, H. J. W., J. T. M. de Jong, D. C. E. Bakker, B. M. Löscher, C. Veth, U. Bathmann, and V. Smetacek (1995), Importance of iron for plankton blooms and carbon dioxide drawdown in the southern ocean, *Nature*, *373*(6513), 412–415, doi:10.1038/373412a0. 2.2.2

DeMaster, D. J. (1981), The supply and accumulation of silica in the marine environment, *Geochimica et Cosmochimica Acta*, *45*(10), 1715–1732, doi:https://doi.org/10.1016/0016-7037(81)90006-5. 2.2.3

DeMaster, D. J. (2002), The accumulation and cycling of biogenic silica in the southern ocean: revisiting the marine silica budget, *Deep Sea Research Part II: Topical Studies in Oceanography*, *49*(16), 3155–3167, doi:https://doi.org/10.1016/S0967-0645(02)00076-0, the Southern Ocean II: Climatic Changes and the Cycle of Carbon. 2.2.3

Devol, A. H., and H. E. Hartnett (2001), Role of the oxygen-deficient zone in transfer of organic carbon to the deep ocean, *Limnology and Oceanography*, *46*(7), 1684–1690, doi:https://doi.org/10.4319/lo.2001.46.7.1684. 1

DeVries, T. (2014), The oceanic anthropogenic co2 sink: Storage, air-sea fluxes, and transports over the industrial era, *Global Biogeochemical Cycles*, *28*(7), 631–647. 2.2.1

DeVries, T., F. Primeau, and C. Deutsch (2012), The sequestration efficiency of the biological pump, *Geophysical Research Letters*, *39*(13). 2.2.1

Donat, M. G., A. D. King, J. T. Overpeck, L. V. Alexander, I. Durre, and D. J. Karoly (2016), Extraordinary heat during the 1930s us dust bowl and associated large-scale conditions, *Climate Dynamics*, *46*(1), 413–426, doi:10.1007/s00382-015-2590-5. 4.2

Ducklow, H. W., D. K. Steinberg, and K. O. Buesseler (2001), Upper ocean carbon export and the biological pump, *Oceanography*, *14*(4), 50–58. 2.2.1

Duteil, O., W. Koeve, A. Oschlies, O. Aumont, D. Bianchi, L. Bopp, E. Galbraith, R. Matear, J. K. Moore, J. L. Sarmiento, and J. Segschneider (2012), Preformed and regenerated phosphate in ocean general circulation models: can right total concentrations be wrong?, *Biogeosciences*, *9*(5), 1797–1807, doi:10.5194/bg-9-1797-2012. 2.2.3

Eyring, V., S. Bony, G. A. Meehl, C. A. Senior, B. Stevens, R. J. Stouffer, and K. E. Taylor (2016), Overview of the coupled model intercomparison project phase 6 (cmip6) experimental design and organization, *Geoscientific Model Development*, *9*(5), 1937–1958, doi:10.5194/gmd-9-1937-2016. 3.1.1

Fahrbach, E., G. Rohardt, M. Schröder, and V. Strass (1994), Transport and structure of the weddell gyre, in *Annales Geophysicae*, vol. 12, pp. 840–855, Springer. 2.1

Fay, A. R., G. A. McKinley, and N. S. Lovenduski (2014), Southern ocean carbon trends: Sensitivity to methods, *Geophysical Research Letters*, *41*(19), 6833–6840. 2.2.1

Fletcher, S. E. M., N. Gruber, A. R. Jacobson, S. C. Doney, S. Dutkiewicz, M. Gerber, M. Follows, F. Joos, K. Lindsay, D. Menemenlis, et al. (2006), Inverse estimates of anthropogenic co2 uptake, transport, and storage by the ocean, *Global biogeochemical cycles*, *20*(2). 2.2.1

Garcia, H., K. Weathers, C. Paver, I. Smolyar, T. Boyer, M. Locarnini, M. Zweng, A. Mishonov, O. Baranova, D. Seidov, et al. (2019a), World ocean atlas 2018, volume 3: Dissolved oxygen, apparent oxygen utilization, and dissolved oxygen saturation. 3.1.2, 3.1.2

Garcia, H., K. Weathers, C. Paver, I. Smolyar, T. Boyer, M. Locarnini, M. Zweng, A. Mishonov, O. Baranova, D. Seidov, et al. (2019b), World ocean atlas 2018. vol. 4: Dissolved inorganic nutrients (phosphate, nitrate and nitrate+ nitrite, silicate). 3.1.2, 3.1.2

Gruber, N., M. Gloor, S. E. Mikaloff Fletcher, S. C. Doney, S. Dutkiewicz, M. J. Follows, M. Gerber, A. R. Jacobson, F. Joos, K. Lindsay, et al. (2009), Oceanic sources, sinks, and transport of atmospheric co2, *Global biogeochemical cycles*, *23*(1). 2.2

Gruber, N., P. Landschützer, and N. S. Lovenduski (2019), The variable southern ocean carbon sink, *Annual review of marine science*, *11*, 159–186. 2.2.1

Hauck, J., A. Lenton, C. Langlais, and R. Matear (2018), The fate of carbon and nutrients exported out of the southern ocean, *Global Biogeochemical Cycles*, *32*(10), 1556–1573. 2.2.4

Hegerl, G. C., S. Brönnimann, A. Schurer, and T. Cowan (2018), The early 20th century warming: Anomalies, causes, and consequences, *WIREs Climate Change*, *9*(4), e522, doi:https://doi.org/10.1002/wcc.522. 4.2

Heinze, C., E. Maier-Reimer, A. M. E. Winguth, and D. Archer (1999), A global oceanic sediment model for long-term climate studies, *Global Biogeochemical Cycles*, *13*(1), 221–250, doi:https://doi.org/10.1029/98GB02812. 3.1.1

Henley, S. F., R. E. Tuerena, A. L. Annett, A. E. Fallick, M. P. Meredith, H. J. Venables, A. Clarke, and R. S. Ganeshram (2017), Macronutrient supply, uptake and recycling in the coastal ocean of the west antarctic peninsula, *Deep Sea Research Part II: Topical Studies in Oceanography*, *139*, 58–76. 2.2.2

Henley, S. F., E. L. Cavan, S. E. Fawcett, R. Kerr, T. Monteiro, R. M. Sherrell, A. R. Bowie, P. W. Boyd, D. K. A. Barnes, I. R. Schloss, T. Marshall, R. Flynn, and S. Smith (2020), Changing biogeochemistry of the southern ocean and its ecosystem implications, *Frontiers in Marine Science*, *7*, doi:10.3389/fmars.2020.00581. 2.2.1, 2.2.1, 2.2.1, 2.2.2

Hofmann, M., and H.-J. Schellnhuber (2009), Oceanic acidification affects marine carbon pump and triggers extended marine oxygen holes, *Proceedings of the National Academy of Sciences*, *106*(9), 3017–3022, doi:10.1073/pnas.0813384106. 2.2.3

Holzer, M., and F. W. Primeau (2013), Global teleconnections in the oceanic phosphorus cycle: Patterns, paths, and timescales, *Journal of Geophysical Research: Oceans*, *118*(4), 1775–1796. 2.2.4

Holzer, M., F. W. Primeau, T. DeVries, and R. Matear (2014), The southern ocean silicon trap: Data-constrained estimates of regenerated silicic acid, trapping efficiencies, and global transport paths, *Journal of Geophysical Research: Oceans*, *119*(1), 313–331. 1, 2.2.4

Honjo, S., S. J. Manganini, R. A. Krishfield, and R. Francois (2008), Particulate organic carbon fluxes to the ocean interior and factors controlling the biological pump: A synthesis of global sediment trap programs since 1983, *Progress in Oceanography*, *76*(3), 217–285, doi:https://doi.org/10.1016/j.pocean.2007.11.003. 1

Ito, T., and M. J. Follows (2005), Preformed phosphate, soft tissue pump and atmospheric co2, *Journal of Marine Research*, *63*(4), 813–839. 1, 2.2.3

Iudicone, D., S. Speich, G. Madec, and B. Blanke (2008), The global conveyor belt from a southern ocean perspective, *Journal of Physical Oceanography*, *38*(7), 1401 – 1425, doi:10.1175/2007JPO3525.1. 1

Iversen, T., M. Bentsen, I. Bethke, J. B. Debernard, A. Kirkevåg, Ø. Seland, H. Drange, J. E. Kristjansson, I. Medhaug, M. Sand, and I. A. Seierstad (2013), The norwegian earth system model, noresm1-m – part 2: Climate response and scenario projections, *Geoscientific Model Development*, *6*(2), 389–415, doi:10.5194/gmd-6-389-2013. 3.1.1

Jaccard, S. L., E. D. Galbraith, A. Martínez-García, and R. F. Anderson (2016), Covariation of deep southern ocean oxygenation and atmospheric co2 through the last ice age, *Nature*, *530*(7589), 207–210, doi:10.1038/nature16514. 2.2.3

Kaiser, M., M. Attrill, S. Jennings, D. Thomas, D. Barnes, A. Brierley, J. Hiddink, H. Kaartokallio, N. Polunin, and D. Raffaelli (2011), *Marine Ecology: Processes, Systems and Impacts*, 2nd ed., Oxford University Press, United Kingdom. 1

Keeling, R. F., and H. E. Garcia (2002), The change in oceanic o₂ inventory associated with recent global warming, *Proceedings of the National Academy of Sciences*, *99*(12), 7848–7853, doi:10.1073/pnas.122154899. 2.2.3

Kennedy, J. J., N. A. Rayner, R. O. Smith, D. E. Parker, and M. Saunby (2011), Reassessing biases and other uncertainties in sea surface temperature observations measured in situ since 1850: 1. measurement and sampling uncertainties, *Journal of Geophysical Research: Atmospheres*, *116*(D14), doi:https://doi.org/10.1029/2010JD015218. 4.2

Keppler, L., and P. Landschützer (2019), Regional wind variability modulates the southern ocean carbon sink, *Scientific reports*, *9*(1), 7384, doi:10.1038/s41598-019-43826-y. 4.2

Khatiwala, S., F. Primeau, and T. Hall (2009), Reconstruction of the history of anthropogenic co2 concentrations in the ocean, *Nature*, *462*(7271), 346–349. 2.1

Khatiwala, S., T. Tanhua, S. Mikaloff Fletcher, M. Gerber, S. C. Doney, H. D. Graven, N. Gruber, G. A. McKinley, A. Murata, A. F. Ríos, and C. L. Sabine (2013), Global ocean storage of anthropogenic carbon, *Biogeosciences*, *10*(4), 2169–2191, doi:10.5194/bg-10-2169-2013. 2.1

Kirkevåg, A., T. Iversen, Ø. Seland, C. Hoose, J. E. Kristjánsson, H. Struthers, A. M. L. Ekman, S. Ghan, J. Griesfeller, E. D. Nilsson, and M. Schulz (2013), Aerosol–climate interactions in the norwegian earth system model – noresm1-m, *Geoscientific Model Development*, *6*(1), 207–244, doi:10.5194/gmd-6-207-2013. 3.1.1

Kirkevåg, A., A. Grini, D. Olivié, Ø. Seland, K. Alterskjær, M. Hummel, I. H. H. Karset, A. Lewinschal, X. Liu, R. Makkonen, I. Bethke, J. Griesfeller, M. Schulz, and T. Iversen (2018), A production-tagged aerosol module for earth system models, osloaero5.3 – extensions and updates for cam5.3-oslo, *Geoscientific Model Development*, *11*(10), 3945–3982, doi:10.5194/gmd-11-3945-2018. 3.1.1

Lauderdale, J. M., A. C. N. Garabato, K. I. C. Oliver, M. J. Follows, and R. G. Williams (2013), Wind-driven changes in southern ocean residual circulation, ocean carbon reservoirs and atmospheric co2, *Climate Dynamics*, *41*(7), 2145–2164, doi:10.1007/s00382-012-1650-3. (document), 2.3

Lin, S., R. W. Litaker, and W. G. Sunda (2016), Phosphorus physiological ecology and molecular mechanisms in marine phytoplankton, *Journal of Phycology*, *52*(1), 10–36, doi:https://doi.org/10.1111/jpy.12365. 1

Margalef, R. (1978), Life-forms of phytoplankton as survival alternatives in an unstable environment, *Oceanologica Acta*, *1*(4), 493–509. 2.2.2

Marinov, I., A. Gnanadesikan, J. Toggweiler, and J. Sarmiento (2006), The southern ocean biogeochemical divide, *Nature*, *441*(7096), 964 – 967, doi:10.1038/nature04883, cited by: 246. (document), 1, 1.1, 1, 2.2, 2.2.1, 2.2.2, 2.2.4, 4.2

Marshall, J., and K. Speer (2012), Closure of the meridional overturning circulation through southern ocean upwelling, *Nature Geoscience*, *5*(3), 171 – 180, doi:10.1038/ngeo1391, cited by: 701. 1

Matear, R. J., and A. C. Hirst (2003), Long-term changes in dissolved oxygen concentrations in the ocean caused by protracted global warming, *Global Biogeochemical Cycles*, *17*(4), doi:https://doi.org/10.1029/2002GB001997. 2.2.3

Matthes, K., B. Funke, M. E. Andersson, L. Barnard, J. Beer, P. Charbonneau, M. A. Clilverd, T. Dudok de Wit, M. Haberreiter, A. Hendry, C. H. Jackman, M. Kretzschmar, T. Kruschke, M. Kunze, U. Langematz, D. R. Marsh, A. C. Maycock, S. Misios, C. J. Rodger, A. A. Scaife, A. Seppälä, M. Shangguan, M. Sinnhuber,

K. Tourpali, I. Usoskin, M. van de Kamp, P. T. Verronen, and S. Versick (2017), Solar forcing for cmip6 (v3.2), *Geoscientific Model Development*, *10*(6), 2247–2302, doi:10.5194/gmd-10-2247-2017. 3.1.1

Mazloff, M. R., P. Heimbach, and C. Wunsch (2010), An eddy-permitting southern ocean state estimate, *Journal of Physical Oceanography*, *40*(5), 880 – 899, doi:10.1175/2009JPO4236.1. 1

Meredith, M. P., and M. A. Brandon (2017), *Oceanography and sea ice in the Southern Ocean*, chap. 8, pp. 216–238, John Wiley and Sons, Ltd, doi:https://doi.org/10.1002/9781118778371.ch8. (document), 2.1

Meredith, M. P., P. L. Woodworth, T. K. Chereskin, D. P. Marshall, L. C. Allison, G. R. Bigg, K. Donohue, K. J. Heywood, C. W. Hughes, A. Hibbert, A. M. Hogg, H. L. Johnson, L. Jullion, B. A. King, H. Leach, Y.-D. Lenn, M. A. Morales Maqueda, D. R. Munday, A. C. Naveira Garabato, C. Provost, J.-B. Sallée, and J. Sprintall (2011), Sustained monitoring of the southern ocean at drake passage: Past achievements and future priorities, *Reviews of Geophysics*, *49*(4), doi:https://doi.org/10.1029/2010RG000348. 2.1

Moore, J. K., W. Fu, F. Primeau, G. L. Britten, K. Lindsay, M. Long, S. C. Doney, N. Mahowald, F. Hoffman, and J. T. Randerson (2018), Sustained climate warming drives declining marine biological productivity, *Science*, *359*(6380), 1139–1143. 2.2, 2.2.2

Morice, C. P., J. J. Kennedy, N. A. Rayner, and P. D. Jones (2012), Quantifying uncertainties in global and regional temperature change using an ensemble of observational estimates: The hadcrut4 data set, *Journal of Geophysical Research: Atmospheres*, *117*(D8), doi:https://doi.org/10.1029/2011JD017187. 4.2

Nelson, D. M., P. Tréguer, M. A. Brzezinski, A. Leynaert, and B. Quéguiner (1995), Production and dissolution of biogenic silica in the ocean: Revised global estimates, comparison with regional data and relationship to biogenic sedimentation, *Global Biogeochemical Cycles*, *9*(3), 359–372, doi:https://doi.org/10.1029/95GB01070. 2.2.3

NorESM2 (2020), 1. cmip6 archive of noresm results — noresm documentation. 3.1.1

Okin, G. S., A. R. Baker, I. Tegen, N. M. Mahowald, F. J. Dentener, R. A. Duce, J. N. Galloway, K. Hunter, M. Kanakidou, N. Kubilay, J. M. Prospero, M. Sarin, V. Surapipith, M. Uematsu, and T. Zhu (2011), Impacts of atmospheric nutrient deposition on marine productivity: Roles of nitrogen, phosphorus, and iron, *Global Biogeochemical Cycles*, *25*(2), doi:https://doi.org/10.1029/2010GB003858. 2.2.2

Olbers, D., and M. Visbeck (2005), A model of the zonally averaged stratification and overturning in the southern ocean, *Journal of Physical Oceanography*, *35*(7), 1190 – 1205, doi:10.1175/JPO2750.1. (document), 2.2

Orr, J. C., E. Maier-Reimer, U. Mikolajewicz, P. Monfray, J. L. Sarmiento, J. Toggweiler, N. K. Taylor, J. Palmer, N. Gruber, C. L. Sabine, et al. (2001), Estimates of anthropogenic carbon uptake from four three-dimensional global ocean models, *Global Biogeochemical Cycles*, *15*(1), 43–60. 2.2.1

Orsi, A. H., T. Whitworth, and W. D. Nowlin (1995), On the meridional extent and fronts of the antarctic circumpolar current, *Deep Sea Research Part I: Oceanographic Research Papers*, *42*(5), 641–673, doi:https://doi.org/10.1016/0967-0637(95)00021-W. (document), 2.1, 4.3

Oschlies, A., W. Koeve, W. Rickels, and K. Rehdanz (2010), Side effects and accounting aspects of hypothetical large-scale southern ocean iron fertilization, *Biogeosciences*, *7*(12), 4017–4035. 2.2.4

Oschlies, A., P. Brandt, L. Stramma, and S. Schmidtko (2018), Drivers and mechanisms of ocean deoxygenation, *Nature Geoscience*, *11*(7), 467–473, doi:10.1038/s41561-018-0152-2. 2.2.3

Pardo, P. C., B. Tilbrook, C. Langlais, T. W. Trull, and S. R. Rintoul (2017), Carbon uptake and biogeochemical change in the southern ocean, south of tasmania, *Biogeosciences*, *14*(22), 5217–5237. 2.2.1

Pellichero, V., J.-B. Sallée, C. C. Chapman, and S. M. Downes (2018), The southern ocean meridional overturning in the sea-ice sector is driven by freshwater fluxes, *Nature communications*, *9*(1), 1789. 2.2.4

Phillips, A. S., C. Deser, and J. Fasullo (2014), Evaluating modes of variability in climate models, *Eos, Transactions American Geophysical Union*, *95*(49), 453–455, doi:10.1002/2014eo490002. (document), 4.13

Pitcher, G. C., A. Aguirre-Velarde, D. Breitburg, J. Cardich, J. Carstensen, D. J. Conley, B. Dewitte, A. Engel, D. Espinoza-Morriberón, G. Flores, V. Garçon, M. Graco, M. Grégoire, D. Gutiérrez, J. M. Hernandez-Ayon, H.-H. M. Huang, K. Isensee, M. E. Jacinto, L. Levin, A. Lorenzo, E. Machu, L. Merma, I. Montes, N. SWA, A. Paulmier, M. Roman, K. Rose, R. Hood, N. N. Rabalais, A. G. V. Salvanes, R. Salvatteci, S. Sánchez, A. Sifeddine, A. W. Tall, A. K. van der Plas, M. Yasuhara, J. Zhang, and Z. Zhu (2021), System controls of coastal and open ocean oxygen depletion, *Progress in Oceanography*, *197*, 102,613, doi:https://doi.org/10.1016/j.pocean.2021.102613. 2.2.3

Pondaven, P., O. Ragueneau, P. Tréguer, A. Hauvespre, L. Dezileau, and J. L. Reyss (2000), Resolving the 'opal paradox'in the southern ocean, *Nature*, *405*(6783), 168–172, doi:10.1038/35012046. 2.2.3

Primeau, F. W., M. Holzer, and T. DeVries (2013), Southern ocean nutrient trapping and the efficiency of the biological pump, *Journal of Geophysical Research: Oceans*, *118*(5), 2547–2564. 1, 1, 2.2.4

Redfield, A. C. (1958), The biological control of chemical factors in the environment, *American scientist*, *46*(3), 230A–221. 2.2.2

Righi, M., B. Andela, V. Eyring, A. Lauer, V. Predoi, M. Schlund, J. Vegas-Regidor, L. Bock, B. Br"otz, L. de Mora, F. Diblen, L. Dreyer, N. Drost, P. Earnshaw, B. Hassler, N. Koldunov, B. Little, S. L. Tomas, and K. Zimmermann (2020), Earth system model evaluation tool (esmvaltool) v2.0 – technical overview, *Geoscientific Model Development*, *13*(3), 1179–1199, doi:10.5194/gmd-13-1179-2020. (document), 4.13

Rintoul, S. R., C. W. Hughes, and D. Olbers (2001), The antarctic circumpolar current system, in *International Geophysics*, vol. 77, pp. 271–XXXVI, Elsevier. 2.1

Roobaert, A., G. G. Laruelle, P. Landschützer, N. Gruber, L. Chou, and P. Regnier (2019), The spatiotemporal dynamics of the sources and sinks of co2 in the global coastal ocean, *Global Biogeochemical Cycles*, *33*(12), 1693–1714. 2.2.1

Sabine, C. L., R. A. Feely, N. Gruber, R. M. Key, K. Lee, J. L. Bullister, R. Wanninkhof, C. Wong, D. W. Wallace, B. Tilbrook, et al. (2004), The oceanic sink for anthropogenic co2, *science*, *305*(5682), 367–371. 2.2.1

Sallée, J.-B., K. Speer, S. Rintoul, and S. Wijffels (2010), Southern ocean thermocline ventilation, *Journal of Physical Oceanography*, *40*(3), 509 – 529, doi:10.1175/2009JPO4291.1. 1

Sallée, J.-B., R. J. Matear, S. R. Rintoul, and A. Lenton (2012), Localized subduction of anthropogenic carbon dioxide in the southern hemisphere oceans, *Nature Geoscience*, *5*(8), 579–584. 2.2.1

Sarmiento, J., N. Gruber, M. Brzezinski, and J. Dunne (2004), High-latitude controls of thermocline nutrients and low latitude biological productivity, *Nature*, *427*(6969), 56 – 60, doi:10.1038/nature02127, cited by: 958. 1, 2.2, 2.2.2, 2.2.4, 4.2

Sarmiento, J. L. (2006), *Ocean biogeochemical dynamics*, Princeton university press. 1

Sarmiento, J. L., and C. Le Quere (1996), Oceanic carbon dioxide uptake in a model of century-scale global warming, *Science*, *274*(5291), 1346–1350. 2.2

Schär, C., P. L. Vidale, D. Lüthi, C. Frei, C. Häberli, M. A. Liniger, and C. Appenzeller (2004), The role of increasing temperature variability in european summer heatwaves, *Nature*, *427*(6972), 332–336, doi:10.1038/nature02300. 4.2

Schmidtko, S., L. Stramma, and M. Visbeck (2017), Decline in global oceanic oxygen content during the past five decades, *Nature*, *542*(7641), 335–339, doi:10.1038/nature21399. 2.2.3

Schubert, S. D., M. J. Suarez, P. J. Pegion, R. D. Koster, and J. T. Bacmeister (2004), On the cause of the 1930s dust bowl, *Science*, *303*(5665), 1855–1859, doi:10.1126/science.1095048. 4.2

Schwinger, J., N. Goris, J. F. Tjiputra, I. Kriest, M. Bentsen, I. Bethke, M. Ilicak, K. M. Assmann, and C. Heinze (2016), Evaluation of noresm-oc (versions 1 and 1.2), the ocean carbon-cycle stand-alone configuration of the norwegian earth system model (noresm1), *Geoscientific Model Development*, *9*(8), 2589–2622, doi:10.5194/gmd-9-2589-2016. 3.1.1

Seland, Ø., M. Bentsen, D. Olivié, T. Toniazzo, A. Gjermundsen, L. S. Graff, J. B. Debernard, A. K. Gupta, Y.-C. He, A. Kirkevåg, J. Schwinger, J. Tjiputra, K. S. Aas, I. Bethke, Y. Fan, J. Griesfeller, A. Grini, C. Guo, M. Ilicak, I. H. H. Karset, O. Landgren, J. Liakka, K. O. Moseid, A. Nummelin, C. Spensberger, H. Tang, Z. Zhang, C. Heinze, T. Iversen, and M. Schulz (2020), Overview of the norwegian earth system model (noresm2) and key climate response of cmip6 deck, historical, and scenario simulations, *Geoscientific Model Development*, *13*(12), 6165–6200, doi:10.5194/gmd-13-6165-2020. 3.1.1, 4.3

Sigman, D. M., M. P. Hain, and G. H. Haug (2010), The polar ocean and glacial cycles in atmospheric co2 concentration, *Nature*, *466*(7302), 47–55. 2.2

Six, K. D., and E. Maier-Reimer (1996), Effects of plankton dynamics on seasonal carbon fluxes in an ocean general circulation model, *Global Biogeochemical Cycles*, *10*(4), 559–583, doi:https://doi.org/10.1029/96GB02561. 3.1.1

Smetacek, V. (1998), Diatoms and the silicate factor, *Nature*, *391*(6664), 224–225. 1

Sokolov, S., and S. R. Rintoul (2009), Circumpolar structure and distribution of the antarctic circumpolar current fronts: 1. mean circumpolar paths, *Journal of Geophysical Research: Oceans*, *114*(C11), doi:https://doi.org/10.1029/2008JC005108. 4.3

Speer, K., S. R. Rintoul, and B. Sloyan (2000), The diabatic deacon cell, *Journal of Physical Oceanography*, *30*(12), 3212 – 3222, doi:10.1175/1520-0485(2000)030<3212:TDDC>2.0.CO;2. (document), 2.2, 2.1

Stramma, L., E. D. Prince, S. Schmidtko, J. Luo, J. P. Hoolihan, M. Visbeck, D. W. R. Wallace, P. Brandt, and A. Körtzinger (2012), Expansion of oxygen minimum zones may reduce available habitat for tropical pelagic fishes, *Nature Climate Change*, *2*(1), 33–37, doi:10.1038/nclimate1304. 1

Sutton, R. T., and D. L. R. Hodson (2005), Atlantic ocean forcing of north american and european summer climate, *Science*, *309*(5731), 115–118, doi:10.1126/science.1109496. 4.2

Takahashi, T., S. C. Sutherland, R. Wanninkhof, C. Sweeney, R. A. Feely, D. W. Chipman, B. Hales, G. Friederich, F. Chavez, C. Sabine, et al. (2009), Climatological mean and decadal change in surface ocean pco2, and net sea–air co2 flux over the global oceans, *Deep Sea Research Part II: Topical Studies in Oceanography*, *56*(8-10), 554–577. 2.2

Takahashi, T., C. Sweeney, B. Hales, D. W. Chipman, T. Newberger, J. G. Goddard, R. A. Iannuzzi, and S. C. Sutherland (2012), The changing carbon cycle in the southern ocean, *Oceanography*, *25*(3), 26–37. 2.2.1

Talley, L. D., G. L. Pickard, W. J. Emery, and J. H. Swift (2011), Chapter 13 - southern ocean, in *Descriptive Physical Oceanography (Sixth Edition)*, edited by L. D. Talley, G. L. Pickard, W. J. Emery, and J. H. Swift, sixth edition ed., pp. 437–471, Academic Press, Boston, doi:https://doi.org/10.1016/B978-0-7506-4552-2.10013-7. 1

Tamsitt, V., H. F. Drake, A. K. Morrison, L. D. Talley, C. O. Dufour, A. R. Gray, S. M. Griffies, M. R. Mazloff, J. L. Sarmiento, J. Wang, and W. Weijer (2017), Spiraling pathways of global deep waters to the surface of the southern ocean, *Nature Communications*, *8*(1), doi:10.1038/s41467-017-00197-0, cited by: 123; All Open Access, Gold Open Access, Green Open Access. 1

Tjiputra, J. F., C. Roelandt, M. Bentsen, D. M. Lawrence, T. Lorentzen, J. Schwinger, Ø. Seland, and C. Heinze (2013), Evaluation of the carbon cycle components in the norwegian earth system model (noresm), *Geoscientific Model Development*, *6*(2), 301–325, doi:10.5194/gmd-6-301-2013. 3.1.1

Tjiputra, J. F., J. Schwinger, M. Bentsen, A. L. Morée, S. Gao, I. Bethke, C. Heinze, N. Goris, A. Gupta, Y.-C. He, D. Olivié, Ø. Seland, and M. Schulz (2020), Ocean biogeochemistry in the norwegian earth system model version 2 (noresm2), *Geoscientific Model Development*, *13*(5), 2393–2431, doi:10.5194/gmd-13-2393-2020. 3.1.1

Toniazzo, T., M. Bentsen, C. Craig, B. E. Eaton, J. Edwards, S. Goldhaber, C. Jablonowski, and P. H. Lauritzen (2020), Enforcing conservation of axial angular momentum in the atmospheric general circulation model cam6, *Geoscientific Model Development*, *13*(2), 685–705, doi:10.5194/gmd-13-685-2020. 3.1.1

Tréguer, P., D. M. Nelson, A. J. V. Bennekom, D. J. DeMaster, A. Leynaert, and B. Quéguiner (1995), The silica balance in the world ocean: A reestimate, *Science*, *268*(5209), 375–379, doi:10.1126/science.268.5209.375. 2.2.3

Tréguer, P. J. (2014), The southern ocean silica cycle, *Comptes Rendus Geoscience*, *346*(11), 279–286, doi:https://doi.org/10.1016/j.crte.2014.07.003. 2.2.3

Tréguer, P. J., and C. L. De La Rocha (2013), The world ocean silica cycle, *Annual Review of Marine Science*, *5*(Volume 5, 2013), 477–501, doi:https://doi.org/10.1146/annurev-marine-121211-172346. 2.2.3

Tréguer, P. J., J. N. Sutton, M. Brzezinski, M. A. Charette, T. Devries, S. Dutkiewicz, C. Ehlert, J. Hawkings, A. Leynaert, S. M. Liu, N. Llopis Monferrer, M. López-Acosta, M. Maldonado, S. Rahman, L. Ran, and O. Rouxel (2021), Reviews and syntheses: The biogeochemical cycle of silicon in the modern ocean, *Biogeosciences*, *18*(4), 1269–1289, doi:10.5194/bg-18-1269-2021. (document), 2.6

van Heuven, S. M., M. Hoppema, E. M. Jones, and H. J. de Baar (2014), Rapid invasion of anthropogenic co2 into the deep circulation of the weddell gyre, *Philosophical Transactions of the Royal Society A: Mathematical, Physical and Engineering Sciences*, *372*(2019), 20130,056. 2.2.1

Verdon-Kidd, D. C., and A. S. Kiem (2009), Nature and causes of protracted droughts in southeast australia: Comparison between the federation, wwii, and big dry droughts, *Geophysical Research Letters*, *36*(22), doi:https://doi.org/10.1029/2009GL041067. 4.2

Wang, B. (2006), *The asian monsoon*, Springer Science & Business Media. 4.2

Wanninkhof, R. (2014), Relationship between wind speed and gas exchange over the ocean revisited, *Limnology and Oceanography: Methods*, *12*(6), 351–362, doi:https://doi.org/10.4319/lom.2014.12.351. 2.2.1, 3.1.1

Watson, A. J., D. Bakker, A. Ridgwell, P. Boyd, and C. Law (2000), Effect of iron supply on southern ocean co2 uptake and implications for glacial atmospheric co2, *Nature*, *407*(6805), 730–733. 2.2.2

Webb, P. (2023), *Introduction to oceanography*, Roger Williams University, Roger Williams University. 2.2.3

Weber, T. S., and C. Deutsch (2010), Ocean nutrient ratios governed by plankton biogeography, *Nature*, *467*(7315), 550–554. 2.2.2

Williams, M. J. M. (2015), *The Southern Ocean*, pp. 115–127, Springer International Publishing, Cham, doi:10.1007/978-3-319-18947-5_7. 1

Williams, R. G., and M. J. Follows (2011), *Ocean dynamics and the carbon cycle: Principles and mechanisms*, Cambridge University Press. (document), 2.3

Xie, Y., V. Tamsitt, and L. T. Bach (2022), Localizing the southern ocean biogeochemical divide, *Geophysical Research Letters*, *49*(8), e2022GL098,260, doi:https://doi.org/10.1029/2022GL098260, e2022GL098260 2022GL098260. 1, 1, 2.2.4, 4.3, 5.1.3

Zhou, T., S. Brönnimann, T. Griesser, A. M. Fischer, and L. Zou (2010), A reconstructed dynamic indian monsoon index extended back to 1880, *Climate Dynamics*, *34*(4), 573–585, doi:10.1007/s00382-009-0552-5. 4.2